

## ARTICLE

# Honeybee $\text{Ca}_v4$ has distinct permeation, inactivation, and pharmacology from homologous $\text{Na}_v$ channels

Anaïs Bertaud<sup>1\*</sup>, Thierry Cens<sup>1\*</sup>, Alain Chavanieu<sup>1</sup>, Sébastien Estaran<sup>1</sup>, Matthieu Rousset<sup>1</sup>, Lisa Soussi<sup>1</sup>, Claudine Ménard<sup>1</sup>, Akelsso Kadala<sup>2</sup>, Claude Collet<sup>2</sup>, Sébastien Dutertre<sup>1</sup>, Patrick Bois<sup>3</sup>, Pascal Gosselin-Badaroudine<sup>4</sup>, Jean-Baptiste Thibaud<sup>1</sup>, Julien Roussel<sup>1</sup>, Michel Vignes<sup>1</sup>, Mohamed Chahine<sup>4</sup>, and Pierre Charnet<sup>1</sup>

DSC1, a *Drosophila* channel with sequence similarity to the voltage-gated sodium channel ( $\text{Na}_v$ ), was identified over 20 years ago. This channel was suspected to function as a non-specific cation channel with the ability to facilitate the permeation of calcium ions ( $\text{Ca}^{2+}$ ). A honeybee channel homologous to DSC1 was recently cloned and shown to exhibit strict selectivity for  $\text{Ca}^{2+}$ , while excluding sodium ions ( $\text{Na}^+$ ), thus defining a new family of  $\text{Ca}^{2+}$  channels, known as  $\text{Ca}_v4$ . In this study, we characterize  $\text{Ca}_v4$ , showing that it exhibits an unprecedented type of inactivation, which depends on both an IFM motif and on the permeating divalent cation, like  $\text{Na}_v$  and  $\text{Ca}_v1$  channels, respectively.  $\text{Ca}_v4$  displays a specific pharmacology with an unusual response to the alkaloid veratrine. It also possesses an inactivation mechanism that uses the same structural domains as  $\text{Na}_v$  but permeates  $\text{Ca}^{2+}$  ions instead. This distinctive feature may provide valuable insights into how voltage- and calcium-dependent modulation of voltage-gated  $\text{Ca}^{2+}$  and  $\text{Na}^+$  channels occur under conditions involving local changes in intracellular calcium concentrations. Our study underscores the unique profile of  $\text{Ca}_v4$  and defines this channel as a novel class of voltage-gated  $\text{Ca}^{2+}$  channels.

## Introduction

DSC1 (*Drosophila* sodium channel 1, or  $\text{Na}_v2$ ) is a voltage-gated ion channel initially identified in the fruit fly *Drosophila* in 1987 based on its sequence homology with vertebrate sodium channels (Ramaswami and Tanouye, 1989; Salkoff et al., 1987). DSC1 expression is predominantly observed in embryonic and adult neurons (Castella et al., 2001; Hong and Ganetzky, 1994), and tissue-specific isoforms exist in the German cockroach (where this channel is called BSC1 [Liu et al., 2001]). However, its expression is largely absent in non-neuronal tissues. In *Drosophila*, DSC1 is also found in olfactory organs such as antenna segments or maxillary palps, where it plays a role in the processing of olfactory information (Kulkarni et al., 2002). These expression features are also found in honeybees, with RT-PCR signals positive in the brain, muscle, antenna, and ganglion but absent in the gut (Gosselin-Badaroudine et al., 2016). Additionally, it has been suggested to be involved in the response to various stresses or insecticides, including DDT and pyrethroids, in both adult and larval stages (Zhang et al., 2013; Rinkevich et al., 2015; Chen et al., 2018; Dong et al., 2014). However, it is important to note that the direct action

of these insecticides on the DSC1 channel itself has not yet been experimentally tested.

DSC1 belongs to the family of 24 transmembrane (TM) helices channels, which are organized into four homologous domains, each containing six TM  $\alpha$  helices. Similar to the other channels from this family, such as voltage-gated  $\text{Na}^+$  and  $\text{Ca}^{2+}$  channels,  $\text{Na}_v$  and  $\text{Ca}_v$ , respectively (Chen-Izu et al., 2015; Catterall, 2000), these domains are split into two subdomains: a voltage-sensor subdomain, comprising the first four (S1–S4)  $\alpha$  helices, with the S4 being the voltage-sensitive element with four to seven positive charges distributed along the helices, and a pore subdomain made of the S5 and S6 helices (that form the pore walls) and a reentrant, the loop connecting these two helices (that makes the channel ionic selectivity filter [SF]). In all these channels, extra- and intracellular loops connecting the helices and the domains play a crucial role in toxin specificity or intracellular channel regulation, among other functions.

Meticulous inspection of the DSC1 amino acids sequences from fly, cockroach, and honeybee (called  $\text{Ca}_v4$ , [Gosselin-Badaroudine et al., 2016]) revealed that, although being more

<sup>1</sup>Institut des Biomolécules Max Mousseron, Université de Montpellier, CNRS, ENSCM, Montpellier, France; <sup>2</sup>INRAE UR 406, Abeilles et Environnement, Domaine Saint Paul—Site Agroparc, Avignon, France; <sup>3</sup>Laboratoire PRéTI, UR 24184—UFR SFA Pôle Biologie Santé Bâtiment B36/B37, Université de Poitiers, Poitiers, France; <sup>4</sup>CERVO Brain Research Centre, Institut Universitaire en Santé Mentale de Québec, Québec City, Canada.

\*A. Bertaud and T. Cens contributed equally to this paper. Correspondence to Charnet Pierre: pierre.charnet@cnrs.fr.

© 2024 Bertaud et al. This article is distributed under the terms of an Attribution–Noncommercial–Share Alike–No Mirror Sites license for the first six months after the publication date (see <http://www.rupress.org/terms/>). After six months it is available under a Creative Commons License (Attribution–Noncommercial–Share Alike 4.0 International license, as described at <https://creativecommons.org/licenses/by-nc-sa/4.0/>).

Table 1. Amino acid sequences of the selectivity filters of different  $\text{Na}_v$  and  $\text{Ca}_v$  channels

Channel	Locus EEEE	Locus DCS
HsCa <sub>v</sub> 1.1	EEEE	DSQE
HsCa <sub>v</sub> 1.2	EEEE	DSED
HsCa <sub>v</sub> 2.1	EEEE	DEQN
HsCa <sub>v</sub> 2.2	EEEE	DAME
HsCa <sub>v</sub> 2.3	EEEE	TEQE
HsCa <sub>v</sub> 3.1	EEDD	DVNG
Am-Ca <sub>v</sub> 4	DEEA	DEED
DSC1	DEEA	NEED
BSC1	DEEA	NEED
Am-Na <sub>v</sub>	DEKA	NEQG

The EEEE locus is the locus responsible for divalent/monovalent selectivity, while the DCS (divalent cation selectivity) is the locus responsible for the selectivity between divalent cations ( $\text{Ba}^{2+}$ ,  $\text{Ca}^{2+}$ ,  $\text{Sr}^{2+}$ ) (Cens et al., 2007). For Ca<sub>v</sub>4, Am-Na<sub>v</sub>, DSC1, and BSC1 the location of the DCS locus is taken relative to the conserved tryptophan in each pore domain.

similar to the Na<sub>v</sub> than to the Ca<sub>v</sub> channels (40–45% and 20–25% homology when compared to mammalian or insect Na<sub>v</sub> or Ca<sub>v</sub> channels, respectively), the DSC1 pore, and more precisely the channel SF, was clearly different from both Na<sub>v</sub> and Ca<sub>v</sub> channels. The selectivity filter is composed of positively or negatively charged amino acids located in each of the four pore domains that form two rings called EEEE and DCS (divalent cation selectivity) loci (Cens et al., 2007; Cibulsky and Sather, 2000; Sather and McCleskey, 2003; Heinemann et al., 1992; Yang et al., 1993; Tang et al., 2014; Hille, 1992a). The EEEE locus plays a major role in the selection between monovalent and divalent cations and contains the DEKA sequence in Na<sub>v</sub> and the EEEE sequence in Ca<sub>v</sub> (see Table 1 for the sequences of the loci in Na<sub>v</sub>, Ca<sub>v</sub>, and DSC1/Ca<sub>v</sub>4 channels). The EEEE and DCS loci in DSC1/Ca<sub>v</sub>4 are different from Na<sub>v</sub>, Ca<sub>v</sub>, DSC1, or BSC1 channels, and contain the sequence of amino acids DEEA and DEED, respectively (see Fig. 1), suggesting a particular ionic selectivity. Moreover, the loop between domains III and IV (LIII–IV), which plays a critical role in Na<sub>v</sub> fast inactivation through a motif of three specific amino acids (IFM in human Na<sub>v</sub>, and MFM in fruit fly or honeybee Na<sub>v</sub> [Gosselin-Badaroudine et al., 2015]), is partly conserved in DSC1 with the homologous sequence MFL in *Drosophila* and in most other arthropods (Cui et al., 2012), including honeybees (Gosselin-Badaroudine et al., 2016). This observation suggests that DSC1 may represent an evolutionary intermediate stage between Ca<sub>v</sub> and Na<sub>v</sub> channels (Dudev and Lim, 2014b). It is conceivable that DSC1 retains the selectivity of a Ca<sub>v</sub> channel while already incorporating the inactivation mechanism typical of a Na<sub>v</sub> channel. These characteristics delineate a novel voltage-gated calcium channel (VGCC) family, which differs in structure, biophysical, and pharmacological aspects from the three previously recognized subfamilies of VGCC namely Ca<sub>v</sub>1, Ca<sub>v</sub>2, and Ca<sub>v</sub>3 (Gosselin-Badaroudine et al., 2016; Dong et al., 2015). Consequently, Gosselin-Badaroudine

et al. [2016] coined the term Ca<sub>v</sub>4 for the honeybee DSC1 ortholog (Gosselin-Badaroudine et al., 2016), a nomenclature that has been subsequently adopted.

Although the ionic selectivity of mammalian Ca<sub>v</sub> and Na<sub>v</sub> channels has been extensively explored through biophysical, molecular, and structural studies (Neumaier et al., 2015; Sather et al., 1994; Sather and McCleskey, 2003 for review), studies focused on the basal metazoan channels, and more precisely, on DSC1, or its cockroach, honeybee, or sea anemone orthologs (Zhou et al., 2004; Dudev and Lim, 2014b; Moran et al., 2015; Gosselin-Badaroudine et al., 2016), are relatively limited (Gosselin-Badaroudine et al., 2016; Dudev and Lim, 2014a; Gur Barzilai et al., 2012). These studies have suggested that various arrangements of the EEEE locus (EEEE, DEKA, DKEA, and DEEA) in the SF can give rise to different relative  $\text{Na}^+/\text{Ca}^{2+}/\text{Ba}^{2+}/\text{K}^+$  permeabilities. However, their specific selectivity profiles and inactivation properties under different experimental conditions received limited analysis (Gosselin-Badaroudine et al., 2016).

The first biophysical study of the DSC1 channel has been carried out in *Xenopus* oocytes with the DSC1 cockroach ortholog of the *Drosophila* channel (BSC1 [Zhou et al., 2004]). However, due to the existence of endogenous  $\text{Ca}^{2+}$ -activated  $\text{Cl}^-$  current in *Xenopus* oocytes, the recordings were mostly conducted using a high  $\text{Ba}^{2+}$  concentration (50 mM), and in the absence of external  $\text{Cl}^-$ , restricting the contaminating chloride conductance to an inward current (outward flux of  $\text{Cl}^-$ ). On the basis of tail current analysis, BSC1 was described as a cation-permeable channel exhibiting slow activation, inactivation, and deactivation kinetics, and displaying a permeability to divalent cations ( $\text{Ca}^{2+}$  and  $\text{Ba}^{2+}$ ) and, to a lesser extent, to monovalent ions ( $\text{Na}^+$ ). A recent work expressing Ca<sub>v</sub>4 (the honeybee DSC1 ortholog) extends this characterization and suggests that Ca<sub>v</sub>4 was not only able to permeate  $\text{Ca}^{2+}$  but was also impermeable to  $\text{Na}^+$  (Gosselin-Badaroudine et al., 2016),  $\text{Na}^+$  permeability was only restored by the DEEA→DEKA mutation in the SF. However, analysis of Ca<sub>v</sub>4 inactivation has never been performed yet, although differences between  $\text{Ba}^{2+}$  and  $\text{Ca}^{2+}$  currents kinetics have been clearly identified.

Therefore, in the present study, we use the intra-oocyte online-BAPTA-injection procedure, which allows us to efficiently inhibit the  $\text{Ca}^{2+}$ -activated  $\text{Cl}^-$  current, and therefore record  $\text{Ca}^{2+}$  and  $\text{Ba}^{2+}$  currents without any contamination. BAPTA injection spares the  $\text{Ca}^{2+}$ -dependent inactivation, at least on Ca<sub>v</sub>1.2 and Ca<sub>v</sub>1.3  $\text{Ca}^{2+}$  channels, which relies on a very local increase in  $\text{Ca}^{2+}$  concentration in the vicinity of the intracellular mouth of the channel.

We demonstrate that DSC1/Ca<sub>v</sub>4 is a high voltage-activated  $\text{Ca}^{2+}$  channel with a high affinity for divalent cations, an inactivation mechanism driven by the MFL motif in the loop III–IV and subjected to an unusual  $\text{Ca}^{2+}$ -dependency. Ca<sub>v</sub>4 is insensitive to both Na<sub>v</sub> and Ca<sub>v</sub> regulators, with the exception of diltiazem and veratrine. While diltiazem reduces  $\text{Ba}^{2+}$  current amplitude and slows inactivation, veratrine, an alkaloid known for slowing Na<sub>v</sub> channel inactivation and deactivation, exerts the opposite effect on Ca<sub>v</sub>4. This unique behavior therefore truly defines Ca<sub>v</sub>4 as a novel class of VGCC.

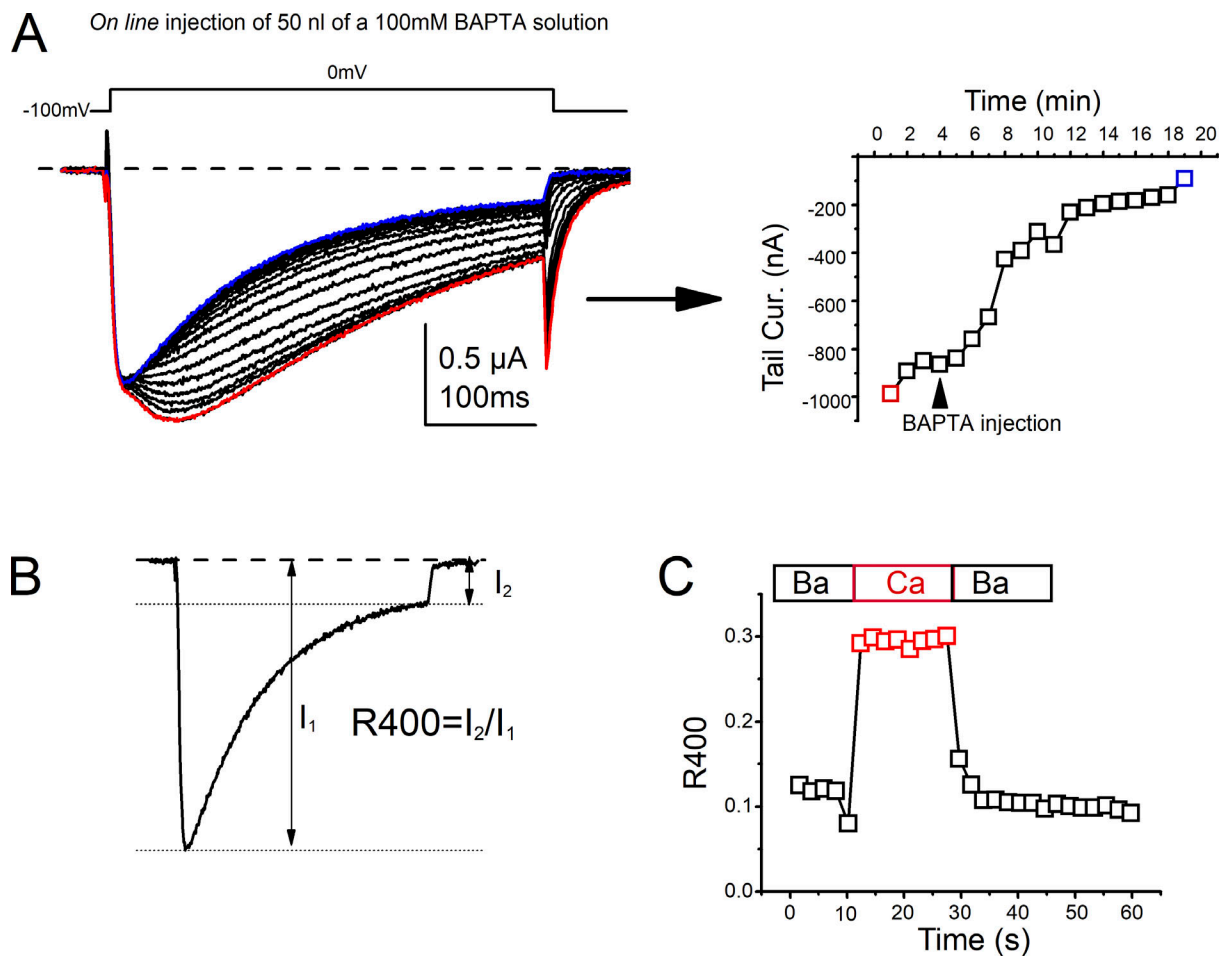


**Figure 1. Effect of online injection of BAPTA on  $Ca_v4$  recordings.** (A) Honeybee  $Ca_v4$  channel activity was recorded in *Xenopus* oocytes during depolarizations from  $-100$  to  $0$  mV in the presence of  $10$  mM  $Ba^{2+}$ . Before any injection (trace in red), a clear biphasic time course and a large inward tail current can be recorded, when current amplitudes are  $>500$  nA. Injection of BAPTA ( $100$  ms,  $2$  Bars,  $100$  mM BAPTA/ $10$  mM HEPES, pH  $7.2$ ) produced a clear decrease in the current amplitude, an acceleration of the kinetics of the tail current, as well as the disappearance of the biphasic time course of the current (compare the red and blue traces). The time required for BAPTA to diffuse and to effectively chelate  $Ca^{2+}$  on the inner side of the membrane is around  $10$ – $15$  min (see the time course of the decrease in the tail current amplitude from the same oocyte on the right), depending on the size of the current and the point of injection. The effects produced by the injection of BAPTA appear faster when the injection is done on the animal pole of the oocyte, where most of the channels are expressed (as can be seen when one does single-channel recordings). The blue trace shows the current at the steady-state effect of BAPTA. BAPTA injection does not impede the development of the Ca-dependent inactivation of  $Ca_v1.2$ ,  $Ca_v2.1$  chimera, or  $Ca_v4$  (CDI and CatCDI, see text and Figs. 3, 6, and 7). (B) Schematic of the quantification of inactivation using R400: the ratio of the current amplitude recorded  $400$  ms after the start of the depolarization ( $I_2$ ) over the peak current amplitude ( $I_1$ ). (C) Time course of the change in the speed of inactivation, quantified with the R400 values, during the switch from a perfusion containing  $10$  mM  $Ba^{2+}$  to a perfusion containing  $10$  mM  $Ca^{2+}$ . At a frequency of stimulation of  $0.5$  Hz, switching from  $Ba^{2+}$  to  $Ca^{2+}$  between two stimulations produces a maximal effect on R400 at the first stimulation after the change.

## Materials and methods

### cDNA, cRNA, and *Xenopus* oocyte preparation

Cloning of Am- $Ca_v4$  channel in the pPol\_Not1 vector, an expression vector containing the T7 promoter, the *Xenopus laevis*  $\beta$ -globin 5'- and -3'-untranslated region, the *Xenopus*  $\beta$ -globin 3'-untranslated regions, and polyA and polyC tracts, was previously done (Gosselin-Badaroudine et al., 2016). The constructs were linearized with Not1, and T7 RNA polymerase was used to synthesize RNA using mMESSAGE mMACHINE T7 kits (Ambion). The Rn $Ca_v1.2$ , Rn $Ca_v2.1$ , DSC1, BSC1, Rn $Ca_v\alpha 2\delta 1$ , and Rn $Ca_v\beta 2a$  channel subunits had the following Genbank accession nos. M67515.1, M64373, AAK01090.1, ABF70206, NP\_037051, and NP\_446303.1, respectively. Sequence alignment was performed with Vector NTI Manager (In Vitrogen). The  $Ca_v2.1$

chimera, harboring the  $Ca_v1.2$  C-end (starting 10 amino acids after the end of the S6 segment of domain IV, AAAAC mutant) was previously described (Cens et al., 2006). Oocyte preparation and injection were also performed (Rousset et al., 2017; Cens et al., 2013, 2015) and carried out in strict accordance with the recommendations and relevant guidelines of our institution. Surgery was performed under anesthesia and efforts were made to minimize suffering. The experimental protocols were approved by the Direction Départementale des Services Vétérinaires (authorization N° C34.16). Briefly, oocytes were surgically removed from anesthetized (using-MS 222, Sigma-Aldrich ref A5040, at  $0.2\%$ ) female *Xenopus* and dissociated with collagenase 1A (ref C9891; Sigma-Aldrich) at  $1$  mg/ml in a low  $Ca^{2+}$  solution (in mM: NaCl,  $82$ ; KCl,  $2$ ;  $MgCl_2$ ,  $1$ ; HEPES,  $5$ ;

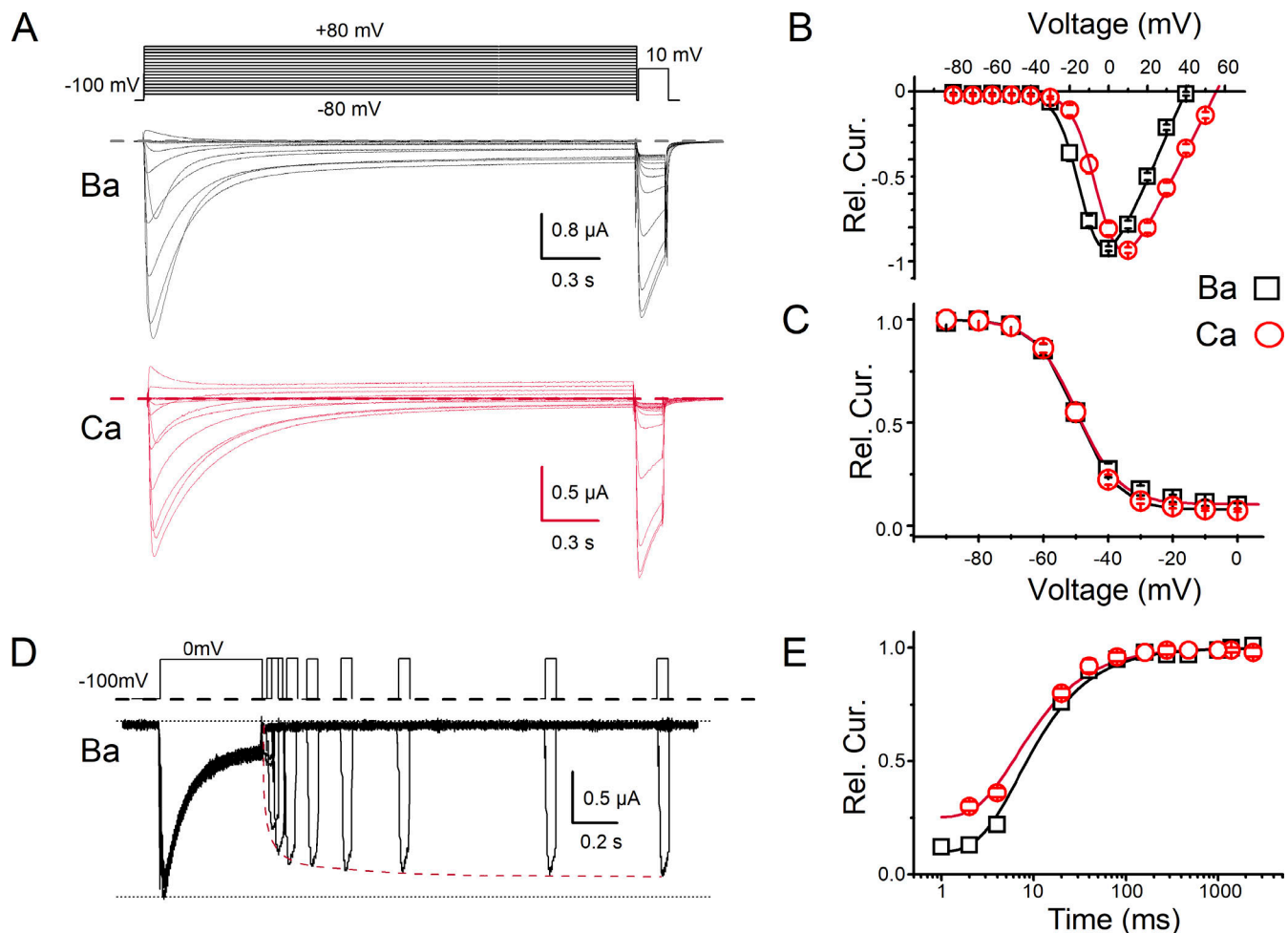


**Figure 2. Basic biophysical properties of honeybee  $Ca_v4$ .** (A) Current traces were recorded in 10 mM  $Ba^{2+}$  (top) or  $Ca^{2+}$  (bottom) -containing solutions during a typical double pulse isochronal inactivation curve protocol. (B and C) Calculated current-voltage curves (B) and isochronal inactivation curves (C) are shown, with recordings made in  $Ba^{2+}$  or  $Ca^{2+}$  in a black square or red circle, respectively. See Table 1 for typical parameters extracted from these curves. (D) Typical current traces recorded during a double pulse protocol with varying time intervals. (E) Measurement of the current amplitude ratio of the second pulse over the first for different time intervals allows constructing the reactivation curves in  $Ba^{2+}$  or  $Ca^{2+}$  and determining both reactivation time constants (see Table 1).

pH = 7.2 with NaOH) for 1.5 h. Batches of ~30 oocytes were then isolated and individually pressure-injected (50–300 ms at 1 bar) with ~30–50 nl of RNA (or cDNA) at a concentration of 1  $\mu$ g/ $\mu$ l. Injected oocytes were kept at 19°C in NDS solution (in mM: NaCl, 96; KCl, 2;  $CaCl_2$ , 1.8;  $MgCl_2$ , 1; HEPES, 5; Na-pyruvate, 2.5; gentamycin, 0.05; pH = 7.2 with NaOH) for 1–3 days before recordings.

#### Electrophysiological recording on *Xenopus* oocytes

For two-electrode voltage-clamp recordings of *Xenopus* oocytes, pipettes (GC150T10; Harvard Electromedical Instruments) of 0.2–1 M $\Omega$  were filled with 3 M KCl. The basic recording solution (BANT10) contained (in mM) BaOH, 10; TEAOH, 20; NMDG, 50; CsOH, 2; and HEPES, 10; pH 7.2 with methanesulfonic acid. In the  $Ca^{2+}$ -containing solution, 10 mM CaOH replaced 10 mM BaOH. The low divalent solution was prepared with (in mM) Na-acetate, 100;  $MgCl_2$ , 2; HEPES, 5; and EGTA, 4; pH 7.2 with NaOH, in which the free  $Ca^{2+}$  concentration was evaluated to be <12.5 nM (WinMaxC, from Chris Patton, Stanford University,

Pacific Grove, CA, USA; [cpatton@stanford.edu](mailto:cpatton@stanford.edu)). The amplifier (Geneclamp 500B, Axon Instruments) was connected to the bath using the virtual ground head stage and agar-KCl (3M) bridges. Junction potentials between the pipettes and the Bant10 solutions were nulled with the two pipettes in the bath before impalement. The holding potential was set to –80 or –100 mV, and depolarizing pulses of different amplitudes and durations were applied every 10 or 15 s, unless otherwise mentioned (see below). The leak and the capacitive transients due to the oocyte membrane were subtracted online using a P/5 procedure of the pClamp acquisition software (Axon Instruments, version 7.0, Molecular Devices). Current traces analysis was performed with Clampfit (Axon Instruments version 10, Molecular Devices).

#### Online BAPTA injection

After the impalement of the two electrodes and the establishment of the voltage clamp, a third microelectrode filled with 100 mM BAPTA and 5 mM HEPES (pH 7.2 with KOH) and connected to a home-made injector was impaled. One or two



Table 2. Current-voltage and -inactivation curve parameters for Cav4 in 10 mM Ba<sup>2+</sup> or 10 mM Ca<sup>2+</sup>

	Barium	Calcium
IV curves		
E <sub>act</sub> (mV)	-11.2 ± 0.9 (40)	-2.5 ± 1.5 (23)
k <sub>act</sub> (mV)	4.4 ± 0.2	5.1 ± 0.2
E <sub>rev</sub> (mV)	39.9 ± 0.7	54.3 ± 1.3
Inactivation curves		
E <sub>in</sub> (mV)	-49.7 ± 0.9 (25)	-49.7 ± 0.1 (16)
K <sub>in</sub> (mV)	6.2 ± 0.2	5.4 ± 0.1
Reactivation curves		
τ (ms)	6.6 ± 0.5 (4)	7.4 ± 1.0 (3)

(x) = number of experiments

pressure pulses (2 bars, 100 ms) were given to inject 10–30 nl of the BAPTA solution and the evolution of the inhibition of the Ca<sup>2+</sup>-activated Cl<sup>-</sup> current was followed on the tail current recorded after a voltage pulse to 0 mV (holding potential -100 mV, see Fig. 1 A). Chelation of Ca<sup>2+</sup> was considered complete when the tail current almost disappeared (<10% of its initial value). Switching from a Ba<sup>2+</sup> to a Ca<sup>2+</sup>-containing solution induced an almost instantaneous change in current inactivation (Fig. 1 B) without any modification of the tail current, indicating the lack of contamination by the Cl conductance.

### Current analysis

Inactivation kinetics were quantified using three methods: calculation of R400 (see Fig. 1 B) or fitting the inactivation phase with decreasing mono- or biexponential equations for short (400) or long (2.5 s pulses), respectively, using Clampfit ver. 10. (Axon Instruments). The equation used for fitting the inactivation phases of the current was for a mono-exponential decay:

$$I = A * e^{-\frac{t}{\tau}} + C,$$

with I, the current amplitude; t, the time; A and τ the amplitude and time constant of the exponential, respectively; and C, the amplitude of the non-inactivating current.

For biexponential decay,

$$I = A1 * e^{-\frac{t}{\tau1}} + A2 * e^{-\frac{t}{\tau2}} + C,$$

where I, the current amplitude; t, the time; A1, A2, and τ1, τ2, the amplitudes and time constants of the slow and fast exponential components, respectively; and C, the amplitude of the non-inactivating current.

The current-voltage curves were obtained by applying 400-ms long depolarizations of -70 to +50 mV (with 10 mV increment) at a frequency of 1/15 s from a holding potential of -80 or -100 mV. The normalized-current voltage curves were fitted using the equation:

$$\frac{I}{I_{max}} = G * \frac{(V - E_{rev})}{1 + \exp\left(\frac{V - E_{act}}{k_{act}}\right)},$$

Table 3. Inactivation curves parameters for Nav1.5, Cav2.1, and Cav1.2 in OR2 (0 mM Ba<sup>2+</sup> or Ca<sup>2+</sup>), 10 mM Ba<sup>2+</sup>, or 10 mM Ca<sup>2+</sup>

	0 Ba/0 Ca	10 Ba
Nav1.5		
E <sub>in</sub> (mV)	-79.8 ± 0.9 (9)	-66.5 ± 1.1 (9)
k <sub>in</sub> (mV)	5.4 ± 0.3	5.2 ± 0.5
10 barium		
10 calcium		
Cav2.1 + Cavβ1		
E <sub>in</sub> (mV)	-38.5 ± 0.2 (5)	-27.4 ± 0.2 (11)
k <sub>in</sub> (mV)	7.7 ± 0.2	6.7 ± 0.2
Cav1.2 + Cavβ2		
E <sub>in</sub> (mV)	-22.9 ± 1.7 (5)	-11.7 ± 1.4 (3)
k <sub>in</sub> (mV)	13.4 ± 2.1	18.7 ± 1.6

(x) = number of experiments

where I and I<sub>max</sub> are the peak-current amplitudes recorded during the voltage step V and at the peak of the current-voltage curve, respectively; G is the normalized macroscopic conductance; E<sub>rev</sub> is the reversal potential; E<sub>act</sub> is the half activation potential; and k<sub>act</sub> is the slope factor.

The normalized isochronal (2.5 s) inactivation curves (also called steady-state inactivation curves) were obtained by applying conditioning depolarizing pulses of 2.5 s in duration and of -80 to +40 mV amplitudes (by 10 mV increment) just before a 400 ms test pulse at +10 mV. The normalized current amplitudes measured during the test pulse were plotted against the voltage of the conditioning pulses. The curves were then fitted using the equation

$$\frac{I}{I_{max}} = R + \frac{(1 - R)}{1 + \exp\left(\frac{V - E_{in}}{k_{in}}\right)},$$

where I and I<sub>max</sub> are the peak-current amplitudes recorded during the voltage step at +10 V for conditioning voltage V and at -80 mV, respectively; R is the fraction of channels that does not inactivate; E<sub>in</sub> is the half inactivation potential, and k<sub>in</sub> is the slope factor.

The reactivation curves were obtained by applying a first 400-ms long depolarization to 0 mV, followed by a return to the holding potential during various durations (t) and a second, 100-ms long, depolarization to 0 mV. The current amplitude recorded during the second depolarization (I<sub>2</sub>) was normalized

Table 4. Half-inactivation potentials in 10 mM Ba<sup>2+</sup> and 10 mM Ca<sup>2+</sup> for the Cav4 mutants

E <sub>in</sub>	Barium	Calcium
Cav4(6)	-23.7 ± 3.5 (8)	-17.5 ± 1.5 (9)
Cav4(8)	-51.1 ± 2.2 (9)	-52.1 ± 1 (8)
Cav4(10)	-29.9 ± 3.5 (17)	-29.1 ± 1 (12)

(x) = number of experiments

Table 5. Current–voltage curves parameters in 10 mM Ba<sup>2+</sup> for the Cav4 mutants

	E <sub>act</sub> (mV)	k <sub>act</sub> (mV)	E <sub>rev</sub> (mV)
Cav4(6)	−11.4 ± 1.2 (22)	4.3 ± 0.2	39.8 ± 1.5
Cav4(8)	−11.2 ± 0.6 (12)	7.9 ± 0.3	38.2 ± 1.9
Cav4(10)	−19.7 ± 1.4 (21)	5.5 ± 0.2	34.9 ± 1.4

(x) = number of experiments

according to the current amplitude recorded during the first depolarization (I<sub>1</sub>) and plotted against the duration t. The curve was then fitted using the following equation:

$$\frac{I_2}{I_1} = R + \frac{(1 - R)}{\exp\left(\frac{t}{\tau}\right)},$$

where R is the proportion of the current that was not inactivated during t, and τ is the time constant of reactivation.

For the cation concentration–conductance curves, the data points were fitted using a hyperbolic Langmuir isotherm function of the following form:

$$\frac{I}{I_{2.5}} = \frac{I_{max}}{Kd + [Ba]},$$

where I is the peak current of the current–voltage curves (using voltage ramps) recorded with a solution at different Ba concentrations; I<sub>2.5</sub> is the peak current of the current–voltage curve recorded when [Ba] = 2.5 mM; I<sub>max</sub> is the estimated maximum current amplitude; Kd is the concentration for half-maximum effect; and [Ba] is the extracellular Ba concentration.

Dose–response curves for Cd<sup>2+</sup> or Ni<sup>2+</sup> were fitted using the dose–response equation of the following form:

$$\frac{I_2}{I_1} = R + \frac{1 - R}{1 + 10^{\left(\frac{pIC_{50} - X}{p}\right)}},$$

where I<sub>2</sub> is the current amplitude measured in the presence of different concentrations of inhibitory divalent cation (Cd<sup>2+</sup> or Ni<sup>2+</sup>); I<sub>1</sub> is the current amplitude measured in the absence of inhibitory cation; R is the fraction of the current that is not affected by the inhibitory cations (close to 0 in these cases); pIC<sub>50</sub> is the log of the inhibitory dose at 50% (IC<sub>50</sub>); X is the log of the inhibitory cation concentrations; and p is a slope factor.

All values were stored in Excel (Microsoft, Office 16), graphs, and their fits were done with Origin (Microcal software, ver 6.0). Statistical tests were performed using Sigmaplot 12.2, and final figures were assembled using Lotus Freelance Graphics 1997 edition. All averaged values are given as mean ± SEM (standard error of the mean). Student's *t* test or Mann–Whitney rank sum test, when normality test failed, or ANOVA were used to assess the differences between mean values, with a statistical significance noted in the figures: \* = *P* < 0.05, \*\* = *P* < 0.01, \*\*\* = *P* < 0.001.

## Results

*Xenopus* oocytes were injected with in vitro synthesized RNA encoding the Am-Cav4 channel isoform previously described

(Gosselin-Badaroudine et al., 2016). Voltage-clamp recordings were made 1–3 days later using 10 mM Ba<sup>2+</sup> as a charge carrier in the extracellular solution. Large inward currents can be recorded in these conditions (see Fig. 1 A), with amplitudes reaching several μA. Such currents induce, most of the time, the appearance of a contaminating Ca<sup>2+</sup>- or Ba<sup>2+</sup>-activated Cl<sup>−</sup> current during both the voltage steps to 0 mV and during the repolarization to −100 mV (seen as a notch and a large tail current, respectively, in the current time-course; see trace in red in Fig. 1 A). This current cannot be efficiently blocked by prior injection of either EGTA, EDTA, or even BAPTA. In our hands, the only procedure that allows us to precisely inhibit this contaminating Cl<sup>−</sup> current is to perform, at the beginning of the recording, an injection of 40–80 nl of a solution containing 100 mM BAPTA and 5 mM HEPES. In these conditions only, we can follow both the inhibition of the contaminating Cl<sup>−</sup> current during both the pulse and the repolarization (Fig. 1). This inhibition required 12–15 min to be complete, as seen by the measurement of the tail current amplitude in the Ba<sup>2+</sup> solution after BAPTA injection (trace in blue, Fig. 1 A). When the steady-state effect of BAPTA is reached, the perfusion of the Ca<sup>2+</sup>-containing solution does not cause any kind of contamination, during either the pulse or the repolarization (see Fig. 1 A). Online injection allows repetition of BAPTA injections if the [Ca]<sub>i</sub> is not properly kept at a low value.

In these conditions, Ba<sup>2+</sup> and Ca<sup>2+</sup> currents can be recorded without any contamination (Fig. 2 A), and current–voltage curves and isochronal inactivation curves can be obtained (Fig. 2, B and C). Notably, the potential for half-activation obtained in 10 mM Ba<sup>2+</sup> (E<sub>act</sub> = −11 ± 1 mV; *n* = 40; see Table 2 for activation and inactivation parameters) distinctly defines Cav4 as a high voltage-activated Ca<sup>2+</sup> channel. The average current amplitude at +10 mV (−2.2 ± 0.3 μA, *n* = 47) 2 days after RNA injection is not affected by the co-expression of *Apis mellifera* of Nav (TEH1-4) or Cav (Cavβ) auxiliary subunits (not shown, but refer to Gosselin-Badaroudine et al., 2016). Perfusion of 10 mM Ca<sup>2+</sup> instead of Ba<sup>2+</sup> induces a shift of the current–voltage curves toward positive voltages by ~10 mV (E<sub>act</sub> varies from −11 to −2.5 mV, Table 2), as expected by a better screening of the surface charges by Ca<sup>2+</sup>, and decreases the peak current amplitude to 1.6 ± 0.3 μA (*n* = 30). However, Ca<sup>2+</sup> has two unexpected effects on channel properties: (1) it does not shift the steady-state inactivation curves, as the curves in Ba<sup>2+</sup> and Ca<sup>2+</sup> superimposed almost perfectly (see Fig. 2 C and Table 1) and (2) it reduces significantly the speed of inactivation, producing an unusual Ca-dependent inactivation with slower kinetics in Ca<sup>2+</sup> than in Ba<sup>2+</sup> (R400 at 0 mV = 0.18 ± 0.03; *n* = 23 and 0.35 ± 0.03; *n* = 17, in Ba<sup>2+</sup> and Ca<sup>2+</sup>, respectively; see Fig. 1 B for R400 calculation and also Fig. 2 A and Fig. 4 B). This slowing of inactivation occurs rapidly and is completely reversible (Fig. 1 C). While inactivation is slowed by Ca<sup>2+</sup>, changing Ba<sup>2+</sup> for Ca<sup>2+</sup> does not change the reactivation time course (Fig. 2 D) with the time constants needed to reactivate the channel being almost similar in Ba<sup>2+</sup> and in Ca<sup>2+</sup> (see Table 2 and Fig. 2 E). Interestingly, the potential for half-inactivation of Cav4 (E<sub>in</sub> = −49 ± 0.6 mV, see Table 2) was more hyperpolarized than that of Ca<sup>2+</sup> channels (Cav1.2 or Cav2.1), but more depolarized than that of Nav channels (Nav1.5),

when recorded in similar conditions,  $E_{in} = -23$ ,  $-38$ , and  $-80$  mV, respectively (see Table 3).

Previous works on Am-Ca<sub>v</sub>4 have evidenced a particular selectivity profile with a high permeability ratio for Ca<sup>2+</sup> over Na<sup>+</sup> (Gosselin-Badaroudine et al., 2016). As expected, the relationship between the current reversal potential and the extracellular Ba<sup>2+</sup> concentrations strictly obey the Nernst law for divalent cations with a slope of 29.5 mV (Fig. 3 A). Moreover, the concentration–conductance curve for Ba<sup>2+</sup> gives a K<sub>d</sub> of  $1.9 \pm 0.4$  mM (Fig. 3 B), which is similar to the value found for the mammalian L type Ca<sub>v</sub>1.2 channel:  $1.9 \pm 0.4$  mM from single channel recordings (Guia et al., 2001) or  $1.1 \pm 0.1$  mM in our conditions (not shown). When mixtures of different Ba<sup>2+</sup>/Ca<sup>2+</sup>

mole fractions were perfused, Ca<sub>v</sub>4 displayed the usual anomalous mole fraction effect (Fig. 3 C for traces and 3 D for graph), consistent with what had been observed with mammalian Ca<sub>v</sub>1.2 or Ca<sub>v</sub>2.1 Ca<sup>2+</sup> channels (Cens et al., 2007). Indeed, the current amplitude displays a marked minimum for low Ca<sup>2+</sup> mole fractions (see the 2 mM Ca<sup>2+</sup> condition marked with an arrow in Fig. 3 D, for example), suggesting that the Ca<sup>2+</sup> binding sites within the channel have a higher affinity for Ca<sup>2+</sup> than for Ba<sup>2+</sup>.

Perfusion of solutions containing either Ba<sup>2+</sup>, Sr<sup>2+</sup>, Ca<sup>2+</sup>, or Na<sup>+</sup> allows depicting more precisely the permeation profile of the channel by calculating averaged current ratios: Ba/Ca =  $1.92 \pm 0.1$  ( $n = 32$ ) and Ba/Sr =  $0.98 \pm 0.07$  ( $n = 5$ ), with almost no Na<sup>+</sup> current flowing through the channel (Fig. 3, E and F). By

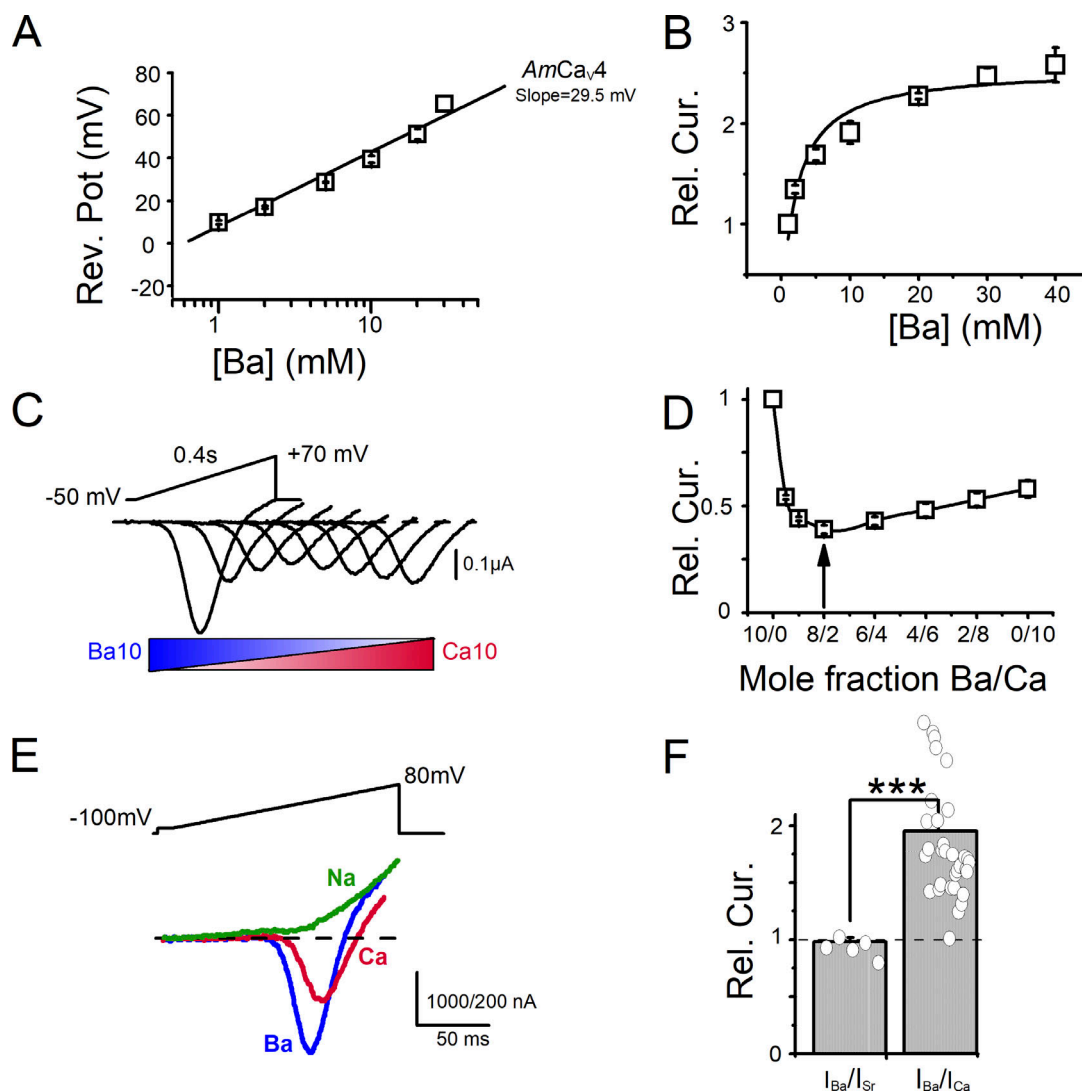


**Figure 3. Permeation properties of Ca<sub>v</sub>4.** (A and B) Analysis of the ionic selectivity for the divalent cation Ba<sup>2+</sup> is shown as a change in the reversal potential in the presence of different concentrations of Ba<sup>2+</sup> (A) or as a current saturation curve for these concentrations (1–40 mM, B). The slope of the reversal potential curve is 29.5 mV, and the K<sub>d</sub> for saturation is  $2.5 \pm 0.1$  mM. (C) Left: Current–voltage curves recorded during the application of voltage ramps (−50/+70 mV duration of 80 ms) in the presence of different Ba/Ca mole fractions (10:1, 9.5:0.5, 9:1, 8:2, 6:4, 4:6, 2:8, and 0:10). Curves are aligned and slightly shifted for visualization. (D) The mole-fraction–peak current amplitude curve of these recordings displays the anomalous current minimum for low doses of Ca<sup>2+</sup>. (E) Current traces recorded during voltage ramps from −100 to +80 mV in solutions containing 10 mM Ba<sup>2+</sup> (blue trace), 10 mM Ca<sup>2+</sup> (red trace), or 100 mM Na<sup>+</sup> (green trace). Note the lack of inward current in the Na<sup>+</sup>-containing solution. (F) Histogram showing the relative peak current amplitude recorded during voltage ramps as in E in solutions containing 10 mM Ba<sup>2+</sup>, 10 mM Ca<sup>2+</sup>, or 10 mM Sr<sup>2+</sup>. The ratios I<sub>Ba</sub>/I<sub>Sr</sub> and I<sub>Ba</sub>/I<sub>Ca</sub> are shown. \*\*\* $P < 0.001$  (Mann–Whitney rank sum test).

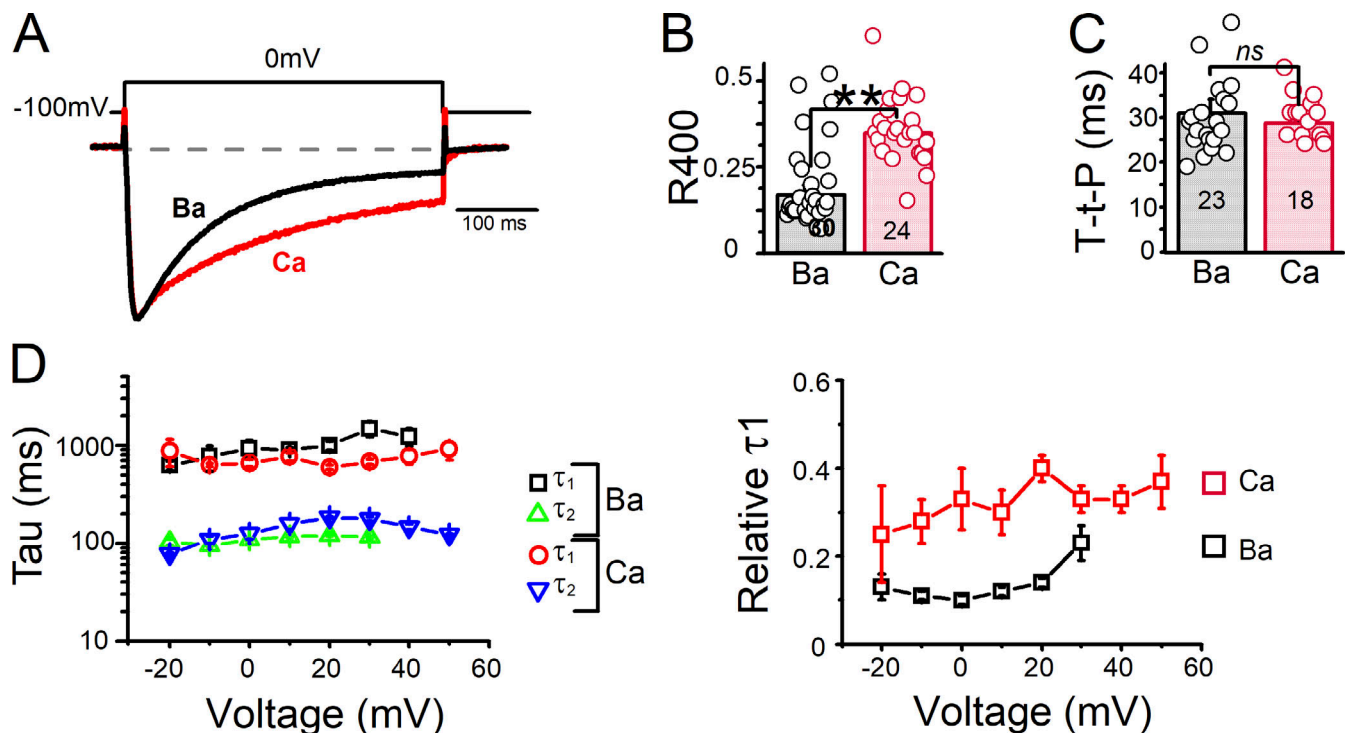


**Figure 4. Inactivation properties of Cav4.** (A) Normalized current traces were recorded for depolarizations from  $-80$  to  $0$  mV in the presence of  $10$  mM Ba<sup>2+</sup> or  $10$  mM Ca<sup>2+</sup>. Note the slowing of inactivation recorded in Ca<sup>2+</sup>. (B and C) Inactivation kinetics, quantified by the calculation of R400 (see Fig. 1B), are slowed by Ca<sup>2+</sup>,  $**P < 0.01$  (Mann–Whitney rank sum test) while the time-to-peak (C) is not affected by the change of the permeant cation ns: non-significant (Mann–Whitney rank sum test,  $P = 0.754$ ). (D) The current inactivation time course, during a  $2.5$ -s long depolarization, can be described as the sum of two exponential functions with a slow time constant,  $\tau_1$ , and a fast time constant,  $\tau_2$ . The change from Ba<sup>2+</sup> to Ca<sup>2+</sup> does not affect the values of these time constants at all the voltages (left) but rather increases the proportion of  $\tau_1$  (right).

measuring the reversal potential measurement in different Ba<sup>2+</sup> and Ca<sup>2+</sup> conditions, the permeability ratio  $P_{Ba}/P_{Ca}$  can be calculated as  $0.54$ , a value slightly larger than the  $P_{Ba}/P_{Ca}$  determined on the mammalian L-type Ca<sup>2+</sup> channel ( $0.4$  [Hille, 1992b]).

As evidenced in Figs. 1 and 2, the switch from the Ba<sup>2+</sup>-containing to the Ca<sup>2+</sup>-containing solution produces a marked slowing of the inactivation time course, better seen when the traces are normalized, as displayed in Fig. 4A. This slowing is obtained in less than a second after exchanging the extracellular solution (Fig. 1C), suggesting a direct impact of the cation on the channel protein itself, and not the involvement of secondary messengers (such as kinases, phosphatases, or PIP2 degradation or synthesis, for example). The slowing can be evaluated by measuring R400, the ratio of the current recorded  $400$  ms after the start of the depolarization over the current recorded at the peak amplitude (see Fig. 1B), and R400 values were significantly smaller for Ba<sup>2+</sup> than for Ca<sup>2+</sup> currents (Fig. 4B). However, interestingly, neither the current activation time-course nor the time-to-peak current was significantly different in Ba<sup>2+</sup> or Ca<sup>2+</sup> (Fig. 4C). Analysis of the current inactivation kinetics during  $2.5$ -s long depolarizations reveals a biexponential time course and shows that this slowing of inactivation occurs without any modification of the values of the two time constants, but rather results from a significant increase in the proportion of the slow time constant of inactivation (Fig. 4D, left and right).

Interestingly, both time constants exhibit almost no voltage-dependence.

This effect of Ca<sup>2+</sup> on Cav4 channel inactivation is puzzling. Na<sub>v</sub> channel inactivation is mediated by the loop located between domains III and IV, which contains a specific sequence of three amino acids—IFM—crucial for rapid inactivation (Kontis et al., 1997; West et al., 1992). Na<sub>v</sub> channels also harbor potential binding sites for Ca<sup>2+</sup> and/or calmodulin (CaM, a Ca<sup>2+</sup>-binding molecule) within the loop III–IV region and on their C-terminal tail that could be involved in Ca<sup>2+</sup>-dependent regulation of Na<sub>v</sub> gating (Johnson, 2020; Salvage et al., 2021), although defining this regulation has proven to be challenging. On the other hand, L-type Ca<sup>2+</sup> channels exhibit a well-documented phenomenon known as Ca<sup>2+</sup>-dependent inactivation (CDI). This occurs when incoming Ca<sup>2+</sup> ions bind to a CaM molecule attached to the L-type Ca channel via CaM-binding sites located on the C-terminal tail of the channel (preIQ and IQ domains) and produces a marked acceleration of the Ca<sup>2+</sup> current inactivation (Peterson et al., 1999; Tadross et al., 2008; Budde et al., 2002; Ben-Johny and Yue, 2014; Ben-Johny et al., 2014). Na<sub>v</sub> and Cav channels also possess putative Ca<sup>2+</sup>-binding sequences (EF-hands) on their C-termini, playing a role in the CDI (at least for Cav1.2 channels), although their capacity for binding Ca<sup>2+</sup> ions is debated. Cav4 channels do possess many of these sequences that are involved in Na<sub>v</sub> and Cav Ca<sup>2+</sup> sensitivity. Putative CaM-binding sites are present on the loop III–IV and the C-terminal



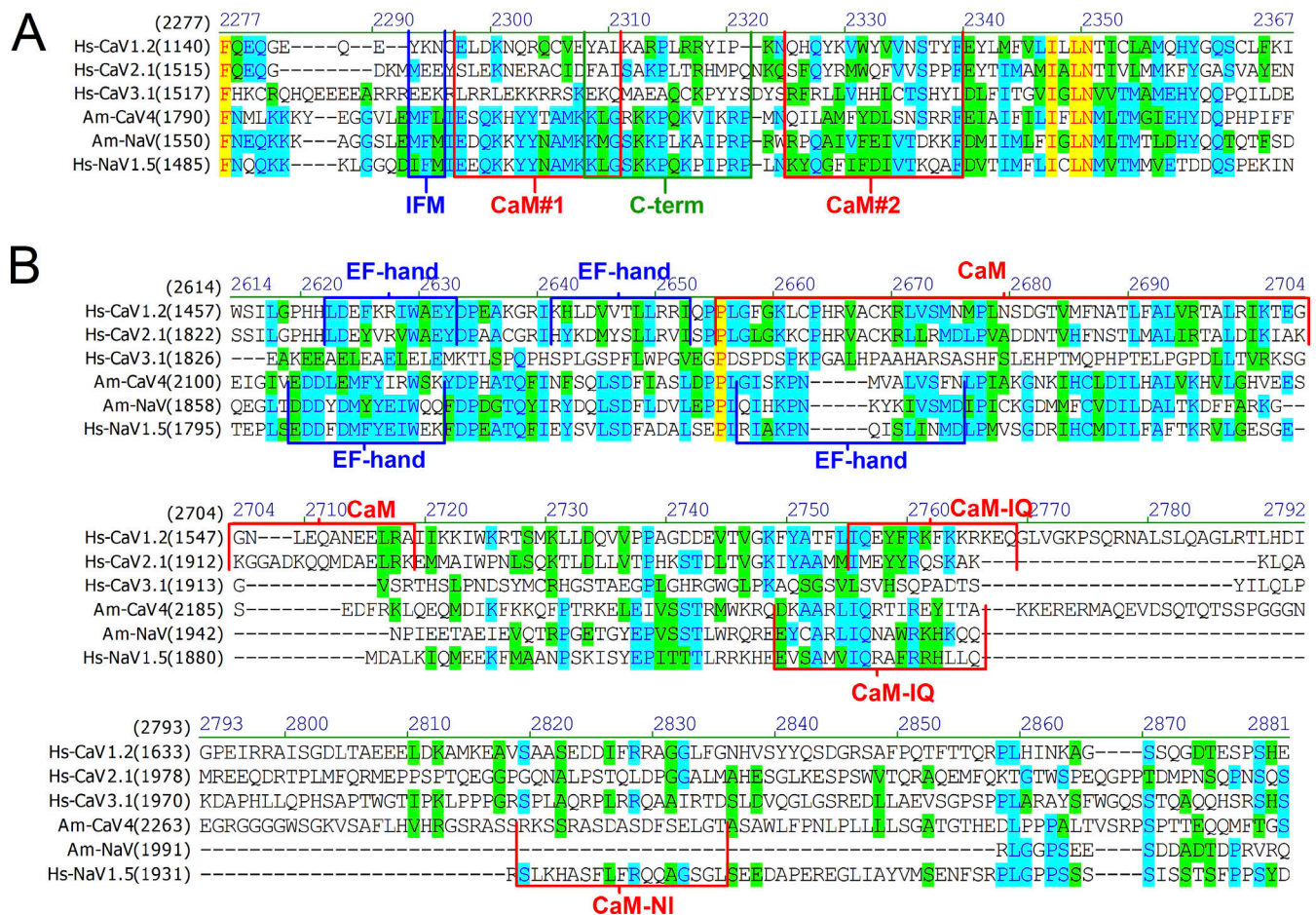


**Figure 5. Primary sequence alignments of the III-IV loop and the proximal C-terminus of Hs-Cav1.2, Hs-Cav2.1, Hs-Cav3.1, Am-Cav4, and Hs-NaV1.5 channels.** (A) Loop III-IV channel sequences. The sequences of the IFM and the binding sites of the C-terminus (C-term) and/or CaM (CaM#1 and CaM#2) are boxed. (B) Alignment of the sequences of the C-terminus of the same channels displaying the location of the EF-hand, the CaM binding sites (CaM), the CaM C-lobe binding (IQ), and the CaM N-lobe binding (CaM-NI). Color code (background/foreground): light blue/deep blue, conservative; green/black: block of similar; yellow/red: identical amino acids.

tail of the Cav4 channel sequence (see Fig. 5, A and B). An MLF sequence, homologous to the IFM sequence found in Nav channels, is also present on the Cav4 sequence, at a localization similar to the IFM in Nav channels, i.e., on the loop III-IV (see Fig. 5 A), and an EF-hand sequence can be found in their proximal C-termini. To investigate the impact of these regions on Cav4 inactivation, we opted to create three Cav4 mutants: one in which the MLF sequence was mutated to AAA (Cav4(6)), another one in which the C-terminal tail was replaced by that of Cav1.2 (Cav4(8)), and a third in which both of these mutations were combined (Cav4(10)). For a visual representation of these mutations, please refer to Fig. 6, B-D. The Cav4(6) mutant does display a complete loss of inactivation at all voltages (Fig. 6, B and E; and Tables 2 and 4 for values), while in the case of the Cav4(8) mutant, the steady-state inactivation parameters are slightly modified compared with those of Cav4 (Fig. 6 C and Tables 2 and 4), although the inactivation time course is slowed. The double mutant, with the modified IFM and C-terminus (Cav4(10)), behaves like the Cav4(6) mutant and shows a complete loss of inactivation. The fact that in these three mutants, the shape of the current-voltage curve (half-activation

potentials, slopes of activation, and reversal potentials (see Fig. 6 F and Table 5) is similar to control values demonstrates that the global functioning of the channel (voltage-dependency of activation and channel selectivity) is preserved and that only inactivation is affected. These results strongly indicate that both sequences are central to the voltage-dependent inactivation of Cav4 and that the MLF sequence undeniably plays a role in Cav4 similar to that played by IFM sequence in Nav channels. Interestingly, with any mutants, the Ca<sup>2+</sup>-dependent slowing of inactivation observed with wild-type Cav4 vanished (as depicted in Fig. 7, A-C), and the R400 values are similar in Ba<sup>2+</sup> and Ca<sup>2+</sup> (Fig. 7 B). Analysis of the Cav4(8) inactivation time constants (the only one that displays a measurable inactivation) reveals that the values are very close in Ba<sup>2+</sup> and in Ca<sup>2+</sup> and close to the values obtained with the wild-type channel (Fig. 4 D and Fig. 7 C). The changes in inactivation for this mutant can be best explained by a change in the proportion of the slow time constant that is clearly larger than that of the wild-type channel at any potentials (~0.4 versus ~0.15, Fig. 4 D and Fig. 7 C). However, as opposed to the wild-type, changing Ba<sup>2+</sup> for Ca<sup>2+</sup> does not modify these values drastically, as seen in Fig. 4 C, explaining the fact

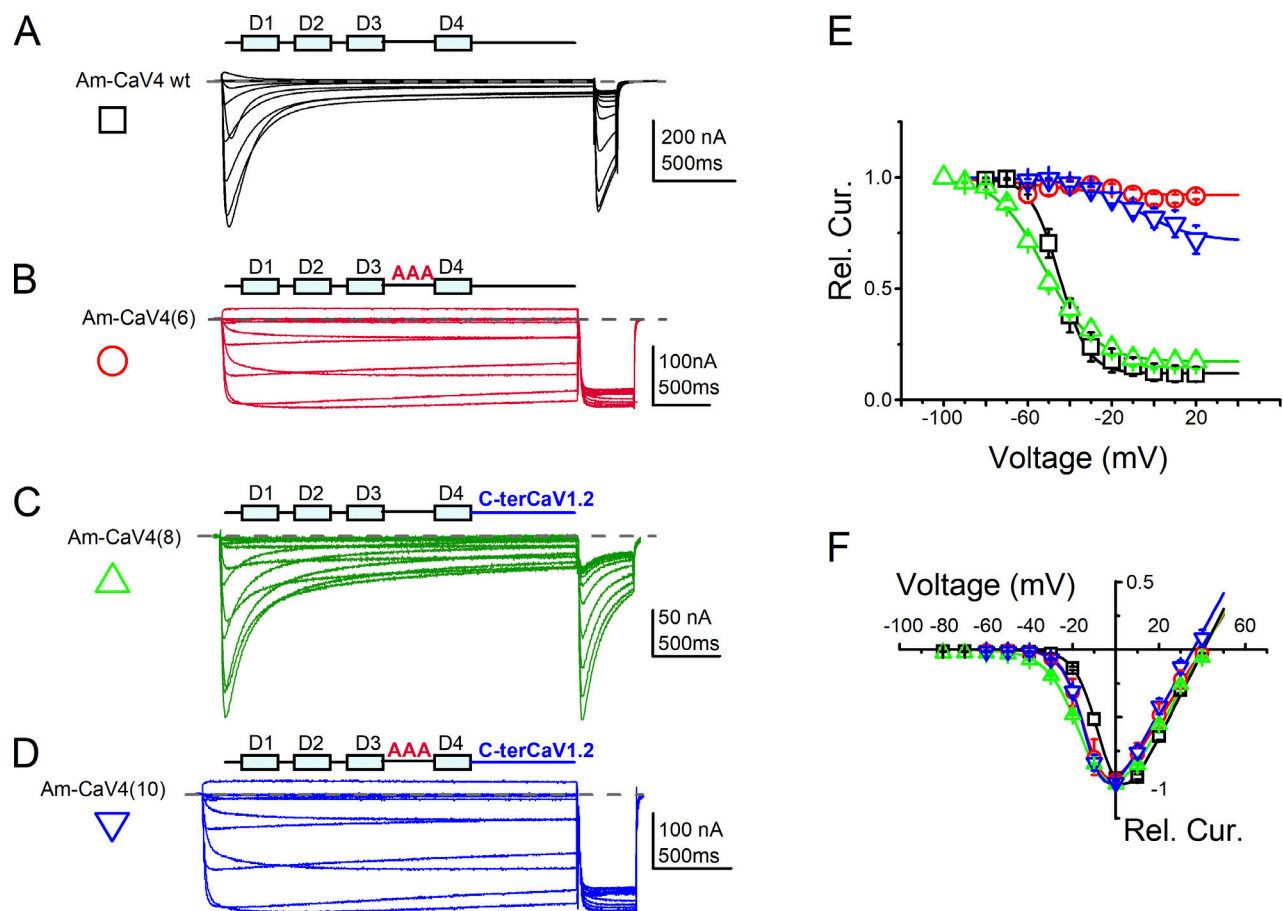


**Figure 6. Use of  $\text{Ca}_v4$  mutants and chimera to study inactivation.** (A)  $\text{Ba}^{2+}$  current traces were recorded during an inactivation protocol as in Fig. 1A with the wild-type  $\text{Ca}_v4$  channel. (B)  $\text{Ca}_v4$  mutant in which the MFL sequence (homologous to the IFM sequence in  $\text{Na}_v$  channels) in domain III-IV was mutated to AAA was generated ( $\text{Ca}_v4(6)$  mutant) and displays completely impaired inactivation kinetics, as shown on the current traces in B, compared with control current traces in A. (C) When the C-terminal tail of  $\text{Ca}_v4$  was exchanged with that of the  $\text{Hs-Ca}_v1.2$  channel, the resulting  $\text{Ca}_v4(8)$  chimera displayed inactivation kinetics notably slower than those of  $\text{Ca}_v4$  (shown on A) but faster than those of the  $\text{Ca}_v4(6)$  chimera (shown on B). (D) The double mutant with both, the MFL and the C-terminal tail modified ( $\text{Ca}_v4(10)$ ), behaves like  $\text{Ca}_v4(6)$ , as seen in D. (E) Isochronal inactivation curves of the wild-type and the three  $\text{Ca}_v4$  mutants are shown in E, and values extracted from the fit are given in Table 3. The different variants of  $\text{Ca}_v4$  use the symbols and colors depicted in A–D. (F) The current–voltage curves of the wild type and the three  $\text{Ca}_v4$  mutants are shown in F and the values extracted from the fit are given in Table 4.

that the R400 values (taken at 0 mV) were identical in these two conditions (Fig. 7B).

To be sure that this cation-dependent inactivation (CatDI) was due to cation binding onto an intracellular target and not on a binding-site located extracellularly, we analyzed the Ca-dependency of the outward current. Outward currents in  $\text{Ba}^{2+}$  and  $\text{Ca}^{2+}$  solutions (probably carried by  $\text{K}^+$ ) were then recorded during depolarization to 0 or +70 mV. While the inward current recorded at 0 mV in  $\text{Ca}^{2+}$  displays the usual slowing of inactivation (when compared to  $\text{Ba}^{2+}$  conditions), the outward current recorded at +70 mV was similar in  $\text{Ca}^{2+}$  and  $\text{Ba}^{2+}$  (see Fig. 8A for current traces and 8B inset for normalized current traces). Statistical analysis of the inactivation time constant at both of these two potentials confirmed the  $\text{Ca}^{2+}$  does not affect current inactivation for positive potential (Fig. 8B).

We then sought to investigate the role of calmodulin in CatDI of  $\text{Ca}_v4$  by coexpressing either wild-type CaM or a mutant invalidated in the four  $\text{Ca}^{2+}$  binding-sites (CaM1234). The results are displayed in Fig. 9, A and C, and demonstrate that CaM does

not play any role in CatDI, since neither CaM nor CaM1234 affect the  $\text{Ca}^{2+}$ -induced changes in the R400 values.

Moreover, the fact that the mutant  $\text{Ca}_v4(8)$ , which exchanges its C-terminus with that of  $\text{Ca}_v1.2$ , does not exhibit a CatDI, while the same substitution in  $\text{Ca}_v2.1$  results in the appearance of the clear real CDI (AAAAC in Fig. 9, B and C) strongly implies that the mechanism of CatDI is distinct despite the involvement of sequences located at similar positions in the channels' primary sequence. A control experiment of the effect of CaM1234 on L-type  $\text{Ca}^{2+}$  channel CDI is shown in Fig. 9D, where CDI is strongly affected by the mutated CaM.

We concluded this characterization by pharmacological profiling of the  $\text{Ca}_v4$ . The dose–response inhibition curves with  $\text{Cd}^{2+}$  and  $\text{Ni}^{2+}$  show 10-fold greater sensitivity to  $\text{Cd}^{2+}$  (respective  $\text{IC}_{50}$  of  $31.9 \pm 2.4$  and  $433.1 \pm 27.3$   $\mu\text{M}$ , Fig. 10A), a specificity commonly observed for high-voltage-activated  $\text{Ca}^{2+}$  channels (Hille, 1992a). The use of a panel of insecticides (permethrin, allethrin, ivermectin, Picrotoxin, fipronil, chlorantraniliprole, and chlothianidin) of  $\text{Ca}_v3$  (mibefradil, NCC-55-0396, TT-A2,

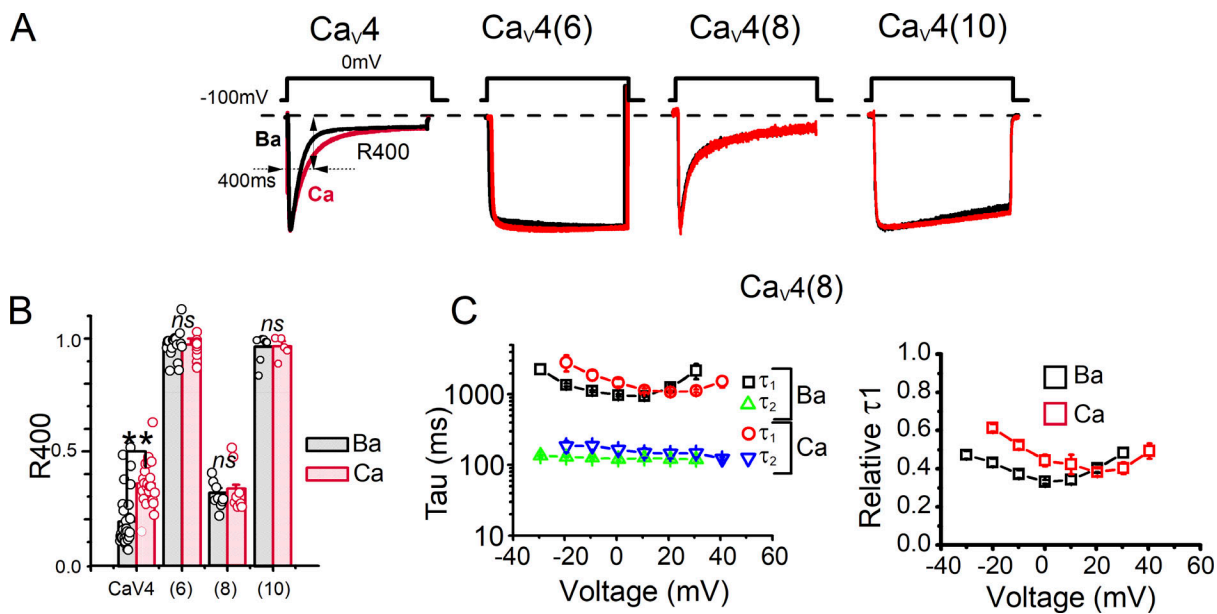


**Figure 7. Inactivation of  $\text{Ca}_v4$  mutants is not Ca dependent.** (A) Superimposed and normalized current traces of the wild type and the three  $\text{Ca}_v4$  mutants recorded in 10 mM  $\text{Ba}^{2+}$  or 10 mM  $\text{Ca}^{2+}$  during depolarizations of 2.5 s showing that the inactivation time course is not affected by the permeant cation. (B) A quantification of the inactivation time-course, shown in B as R400 values, in Ba or Ca, for these mutants, demonstrates the lack of CatDI (respective Mann-Whitney rank sum test P values for the mutants are 0.397, 1.000, and 0.876, respectively). (C) Analysis of the inactivation time constant for the  $\text{Ca}_v4(8)$  mutant ( $n = 13$  and  $11$  for  $\text{Ba}^{2+}$  and  $\text{Ca}^{2+}$ , respectively) shows that neither the time constants (slow time constant:  $\tau_1$ , fast time constant:  $\tau_2$ ) nor their relative amplitude are markedly affected by the permeant cation, as opposed to the wild-type channel (see Fig. 4).

amiloride),  $\text{Ca}_v1$  modulators (nifedipine, PN200-110, Bay-K8644, verapamil, diltiazem), and of toxins and venom (SNX-482, atrachotoxin HV1a, *Thomisus honustus* and *Synema globosum* venoms, and PTx-II) was quite ineffective, except for diltiazem, which is responsible for significant inhibition of the peak current at  $20 \mu\text{M}$  ( $49 \pm 3\%$ ,  $n = 3$ , Fig. 10 B).

We also investigated the effect of several  $\text{Na}_v$  channel modulators. Some of them, such as the pyrethroids (see Fig. 8 B) and TTX (see Gosselin-Badaroudine et al., 2016) were ineffective, but veratrine, an alkaloid mixture extracted from the plant *Veratrum album*, induced a small inhibition of the current amplitude ( $13\% \pm 0.3$ ,  $n = 12$ , when perfused at  $30 \mu\text{M}$ ), and a well-resolved acceleration of current inactivation. Indeed, R400 decreases to 50% of its control value ( $R400 = 0.2 \pm 0.03$  [ $n = 12$ ] to  $0.10 \pm 0.01$  [ $n = 12$ ] for control and veratrine, respectively, Mann-Whitney rank sum test P value = 0.004, see Figs. 10 and 11). At a stimulation frequency of 0.5 Hz, this acceleration develops with a time-constant of 8.2 s, a little faster than the time-constant required for the change in current amplitude (17 s, not shown). The acceleration of inactivation was almost fully reversible, while the effect on the current amplitude was not (Fig. 11 B). A similar effect was obtained in the presence of  $\text{Ca}^{2+}$  in the perfusion medium instead of  $\text{Ba}^{2+}$  (Fig. 12). During these short depolarizations, a condition necessary to carry out dose-response curves of veratrine, the inactivation time course can be better estimated by a fit with a single exponential. Increasing veratrine concentration decreases the  $\text{Ca}_v4$  inactivation time constant in a dose-dependent manner (Fig. 11, A-C), and a similar effect was also obtained with the mutant channel  $\text{Ca}_v4(6)$ . While the  $\text{Ca}_v4(6)$  inactivation time constant was too large to be effectively

measured for low doses of veratrine, the perfusion of high doses increases the inactivation up to the values recorded for the wild type at similar doses (at  $100 \mu\text{M}$ , see Fig. 11 C). Interestingly, outward current time constants are smaller than the inward current but do not vary between  $-40$  and  $+110$  mV (not shown). On outward currents, veratrine has a tendency to decrease the time constant of inactivation down to values close to that obtained for the inward current ( $59.5 \pm 2.5$  and  $58.9 \pm 5.7$  ms for control and veratrine traces at  $+70$  mV, respectively, see histogram Fig. 13), but this effect does not reach a significant level (Mann-Whitney rank sum test P value = 0.057). Similar effects were produced with veratridine, which is the major component of veratrine (not shown), and the effects were undoubtedly different from those produced by veratrine or veratridine on  $\text{Na}_v$  channels, for which a marked slowing of current inactivation and deactivation were reported without noticeable effects on the peak current (Sutro, 1986; Sigel, 1987), and the effects that were also retrieved with the honeybee  $\text{Na}_v$  channel expressed in *Xenopus* oocytes (not shown). Altogether, these effects seem to indicate that the veratrine-induced acceleration of inactivation is independent of the usual MFL-gated inactivation and involves other mechanisms. In the absence of other specific biophysical or pharmacological markers of  $\text{Ca}_v4$ , veratrine could be used as a pharmacological tool to reveal the presence of  $\text{Ca}_v4$  in situ, in muscles or neurons for instance.

## Discussion

To achieve a more comprehensive understanding of cellular excitability in honeybees and their sensitivity to pesticides, our



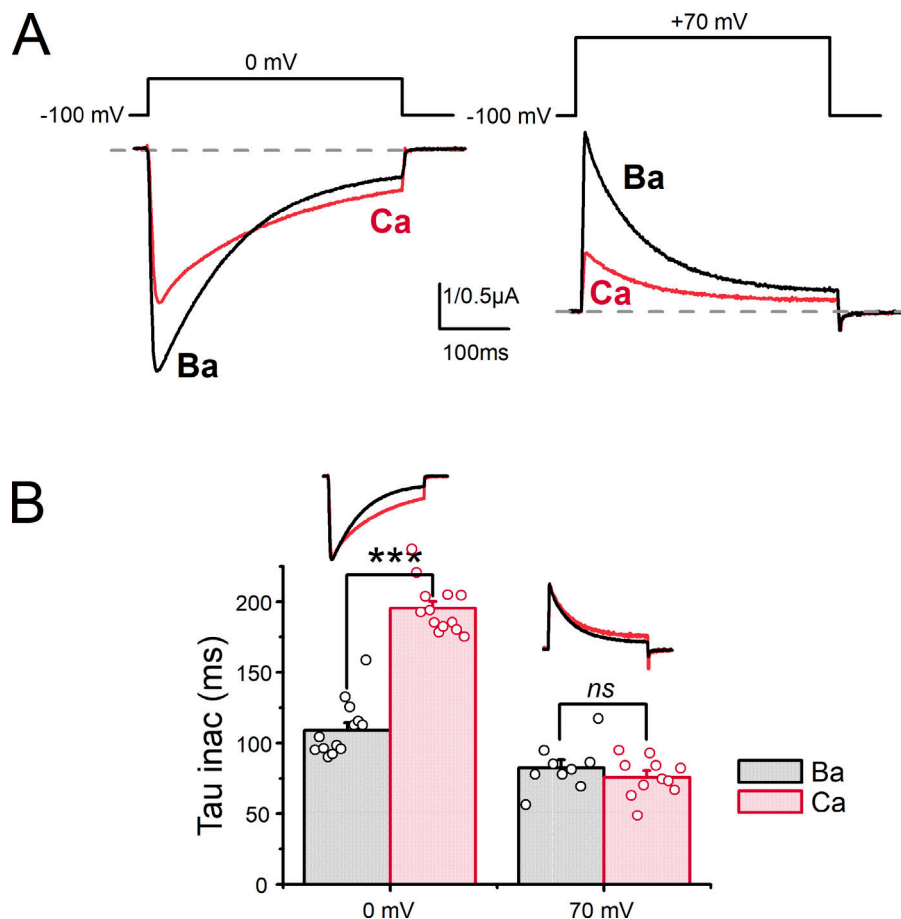


**Figure 8. Ca-dependent inactivation is limited to inward current. (A)** Superimposed current traces of the wild-type Cav4 channel in the presence of Ba<sup>2+</sup> (in black) or Ca<sup>2+</sup> (in red) were recorded during depolarizations to 0 (left) or +70 mV (right). **(B)** Histogram showing the averaged time constants of inactivation measured at 0 or +70 mV in Ca<sup>2+</sup> or Ba<sup>2+</sup> (10 mM). Insets show the normalized current traces. \*\*\* denotes statistically different values (Mann-Whitney rank sum test,  $P < 0.001$ ), ns, not statistically significant (Student's  $t$  test,  $P = 0.316$ ).

research group has been actively engaged in identifying and cloning ion channels expressed in larvae and adult bees. We have previously published preliminary characterizations of the ligand-gated RDL, glutamate and nicotinic receptors, and the voltage-gated Cav1, Cav2, Cav3, Cav4, and Nav1 channels (Cens et al., 2015; Gosselin-Badaroudine et al., 2017; Cens et al., 2013; Gosselin-Badaroudine et al., 2016; Rousset et al., 2017; Gosselin-Badaroudine et al., 2015; Collet et al., 2016; Brunello et al., 2022). Cav4, a channel homologous to *Drosophila* DSC1, did not conform to the classical Nav channel archetype, and neither its biophysical nor pharmacological properties allowed us to classify this channel in any of the three already established Cav channel subfamilies (Cav1, Cav2, and Cav3). Consequently, we proposed the existence of a novel class of Ca<sup>2+</sup> channel termed Cav4 (Gosselin-Badaroudine et al., 2016). In this study, we provided evidence demonstrating that the Cav4 channel exhibits distinctive characteristics with regard to cation permeability, voltage dependency, Ca<sup>2+</sup>-dependent inactivation mechanisms, and pharmacological properties.

#### Cav4 channel permeation and selectivity

The results depicted in Figs. 2 and 3 unequivocally demonstrate that Cav4 is a high-voltage activated Ca<sup>2+</sup> channel that permeates both Ca<sup>2+</sup> and Ba<sup>2+</sup> and exhibits an anomalous mole fraction between Ba<sup>2+</sup> and Ca<sup>2+</sup>, suggesting a higher selectivity for Ca<sup>2+</sup>. Moreover, the Cav4 saturation curves for divalent cations (Fig. 3) and the higher sensitivity to Cd<sup>2+</sup> versus Ni<sup>2+</sup> are typical

of HVA Ca<sup>2+</sup> channels (Guia et al., 2001). The shift of the current-voltage curve observed upon extracellular cations changes (Fig. 2) is also reminiscent of that observed in mammalian Cav1.2 or Cav2.1 Ca<sup>2+</sup> channels, for example.

Na<sup>+</sup> ions were unable to permeate Cav4 even in the presence of EGTA in the extracellular solution, consistent with our previous findings (Gosselin-Badaroudine et al., 2016). While channels harboring a Ca<sup>2+</sup> or Ba<sup>2+</sup> channel permeability with DEEA selectivity filters have been described in Cnidaria (Gur Barzilai et al., 2012), *Drosophila*, and cockroach (Zhou et al., 2004), these channels retained a permeability to Na<sup>+</sup> in the absence of Ca<sup>2+</sup> or Ba<sup>2+</sup>, which is not the case here.

The sequences of the SF at both loci (EEEE and DCS) identified in Nav and Cav channels (Heinemann et al., 1992; Cens et al., 2007; Neumaier et al., 2015) are unique in Cav4, with three negative charges at the EEEE locus, DEEA (numbered position 0) and four negative charges at the DCS locus (DEED; see Table 1 for the SF sequences of different Cav and Nav channels). The presence of these negative charges pointing toward the pore at the DCS locus (Wu et al., 2016) is known to affect the selectivity for monovalent cations in Nav channels (Heinemann et al., 1992) and lightly those of divalent cations in the Cav. Therefore, the fact that four negative charges are found in Cav4 but not in the DSC1, BSC1, or other Nav or Cav channels (Table 1) could explain the differences in Na permeability between these channels. The aspartate at position +1 (relative to the E in the SF of domain II) and the glutamate at position 0 of domain IV (conserved in all



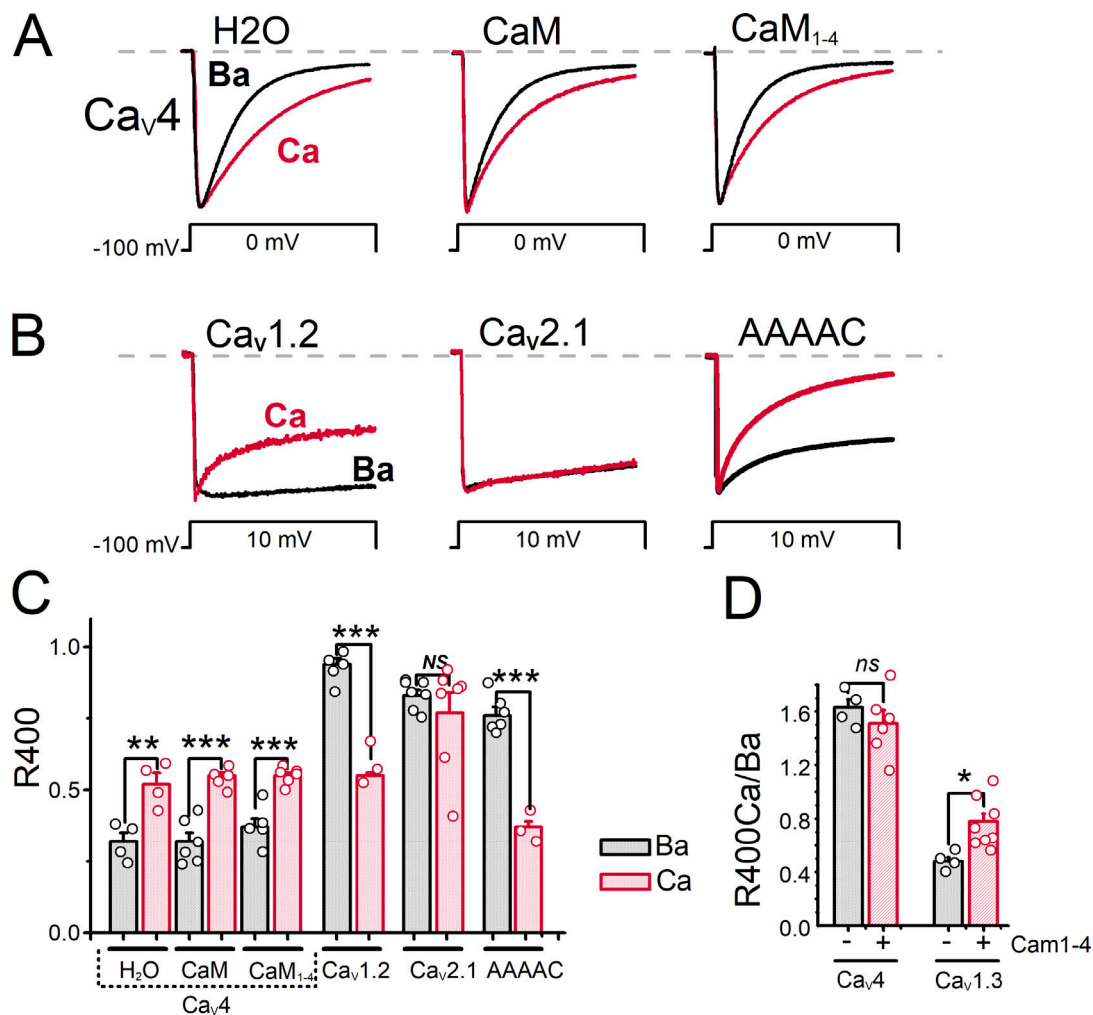


**Figure 9. Effect of calmodulin (CaM) and the Ca-insensitive calmodulin mutant (CaM1234) on Cav4 inactivation (CatDI).** *Xenopus* oocytes were injected with the Cav4 channel cRNA and either water, CaM, or CaM1234 cRNA, and currents were recorded 2–3 days later using Ba<sup>2+</sup> or Ca<sup>2+</sup> solutions. **(A)** Superimposed normalized current traces of the Cav4 channel alone or coexpressed with CaM or CaM1234 were recorded in 10 mM Ba<sup>2+</sup> (black traces) or 10 mM Ca<sup>2+</sup> (red traces) during depolarizations of 400 ms. Note that in each case, the current inactivation is slowed by the perfusion of the Ca solution (red traces). **(B)** When a Ca-insensitive Cav2.1 channel exchanges its C-terminal tail with that of the Cav1.2-sensitive channel, the resultant channel (AAAAC) displays a clear Ca-dependent acceleration of inactivation similar to the Cav1.2 channel (black traces in Ba<sup>2+</sup>, red traces in Ca<sup>2+</sup>). **(C)** R400 values were calculated for these different conditions as depicted in A and B in 10 mM Ba<sup>2+</sup> or 10 mM Ca<sup>2+</sup>. Note that CaM and CaM1234 had no effect on Cav4 inactivation. The Cav1.2 C-terminus blocked the Ca-dependent inactivation of Cav4 (see Fig. 6), induced a new Ca-dependent inactivation on Cav2.1 channels (respective Student's *t* test *P* values: 0.004; 0.0004; 0.00008; 0.00019; Mann–Whitney rank sum test *P* = 0.902, and Student's *t* test *P* = 3.18 × 10<sup>−7</sup>). **(D)** The ratio of Ca-dependent inactivation (R400 obtained in Ca<sup>2+</sup> divided by R400 obtained in Ba<sup>2+</sup>) of Cav4 is not affected by the coexpression of CaM1234, while CaM1234 strongly decreases this ratio in the case of Cav1.3 (Student's *t* test, *P* = 0.384 and 0.0241).

Ca<sub>v</sub> channels [Abderemane-Ali et al., 2019; Shaya et al., 2014] but replaced by tryptophan and alanine, respectively, in Cav4) may also play a role in this particular selectivity. Substituting the (+1)-aspartate by non-charged amino acids in Cav1.2 did not alter the reversal potential in the presence of divalent cations (Abderemane-Ali et al., 2019) but affected the channel kinetics. Whether this aspartate impacts the permeation of monovalent cation has not been examined.

The observation that divalent cations can permeate, whereas smaller monovalent Na<sup>+</sup> ions (respective size of 1.35 Å for Ca<sup>2+</sup>, 0.99 Å, for Ba<sup>2+</sup> and 0.95 Å for Na<sup>+</sup>) cannot do so in their absence could also be attributed to the blockade of the inward monovalent

current by extracellular Mg<sup>2+</sup>, present in the low Ca solution and not effectively chelated by EGTA.

Positions 0 (EEEE locus), +1 (aspartate), and/or +4 (DCS locus) are thus pertinent candidates for the strict selectivity of Cav4 to divalent cations. However, the definitive proof of their involvement in specific cation coordination in the Cav4 pore will require additional mutagenesis studies. In any case, the Cav4 selectivity pattern is a novel feature in the Ca<sub>v</sub> family, and future structural studies on Cav4 may provide important new information on the role of these amino acids in the formation and properties of the cation binding sites and the Ca<sup>2+</sup> coordination in Cav4 pore.

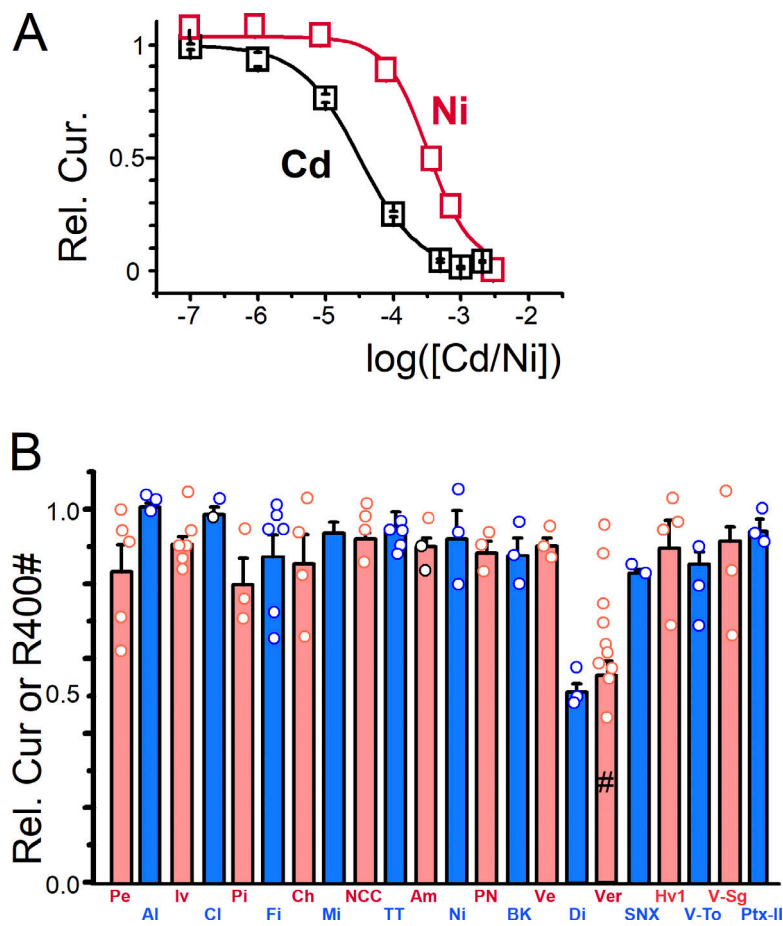


**Figure 10. Pharmacological properties of  $\text{Ca}_v4$ .** (A) Dose-response curves for  $\text{Cd}^{2+}$  (black squares) or  $\text{Ni}^{2+}$  (red squares) were recorded using depolarizations from  $-80$  to  $0$  mV in the presence of  $10$  mM  $\text{Ba}^{2+}$ . Experimental data points are fitted using a hyperbolic Langmuir isotherm function, and extracted  $\text{IC}_{50}$  values are  $31.2 \pm 2.4$   $\mu\text{M}$  ( $n = 5$ ) and  $433.1 \pm 27.3$   $\mu\text{M}$  ( $n = 5$ ) for  $\text{Cd}^{2+}$  and  $\text{Ni}^{2+}$ , respectively. (B) Effect of various  $\text{Na}_v$  or  $\text{Ca}_v$  inhibitors, as well as some toxins or insecticides, on the current amplitude or the R400 (noted # for veratrine) generated by the  $\text{Ca}_v4$  channel. Note that almost none of these drugs have an effect on  $\text{Ca}_v4$ . The drugs tested are from left to right: permethrin (50  $\mu\text{M}$ ), allethrin (50  $\mu\text{M}$ ), ivermectin (10  $\mu\text{M}$ ), clothianidin (10  $\mu\text{M}$ ), picotoin (10  $\mu\text{M}$ ), fipronil (10  $\mu\text{M}$ ), chlorantraniliprole (10  $\mu\text{M}$ ), mibefradil (10  $\mu\text{M}$ ), NCC-55-0396 (20  $\mu\text{M}$ ), TTA-A2 (1  $\mu\text{M}$ ), amiloride (1 mM), nifedipine (10  $\mu\text{M}$ ), PN200-110 (10  $\mu\text{M}$ ), BayK-8644 (10  $\mu\text{M}$ ), verapamil (10  $\mu\text{M}$ ), diltiazem (20  $\mu\text{M}$ ), veratrine (30  $\mu\text{M}$ ), SNX-482 (10  $\mu\text{M}$ ), atrachotoxine Hv1 (1  $\mu\text{M}$ ), thomisus venom (1/50), *Synema globosum* venom (1/50), and PLTX-II (1  $\mu\text{M}$ ). A significant effect is obtained only with diltiazem and veratrine.

### $\text{Ca}_v4$ channel inactivation

The sequence similarities between  $\text{Ca}_v4$  and  $\text{Na}_v$  channels extend to the loop connecting domains III and IV and, in particular, to the IFM sequence known to be crucial for  $\text{Na}_v$  fast inactivation. Hydrophobic interactions between the IFM sequence and the S4-S5 linkers of DIII and DIV and part of the activation gate at the bottom of the DIV-S6 stabilize the pore in a closed-inactivated conformation (a mechanism formerly called hinged-lid [Catterall, 2013; Jiang et al., 2020; Liu et al., 2023]). The IFM sequence is replaced by MFM and MFL in honeybee  $\text{Na}_v$  and  $\text{Ca}_v4$  channels, respectively.  $\text{Ca}_v4$  inactivation kinetics (100–1,000 ms) are slower than those of honeybee or mammalian  $\text{Na}_v$  channels (2–10 ms [Fux et al., 2018]) and are not affected by the membrane potential. Moreover,  $\text{Ca}_v4$  steady-state inactivation appears to be insensitive to surface charge density, as opposed to the voltage dependence of activation. Inactivation was also noticeably slower in  $\text{Ca}^{2+}$  compared with  $\text{Ba}^{2+}$ . All of these features are specific to  $\text{Ca}_v4$  and are not observed in other  $\text{Ca}_v$  or  $\text{Na}_v$  channels (see Figs. 2, 3, and 4).

Interestingly, the MFL to AAA substitution (as the  $\text{Ca}_v4(6)$  mutant, and as shown in Fig. 6) completely abolishes fast inactivation, suggesting a potential shared mechanism with  $\text{Na}_v$  channels (Zhou et al., 2004; Catterall, 2013). The observation that the inactivation kinetics are not voltage-dependent can be explained by a voltage-independent gating step that acts as the rate-limiting factor in the inactivation process. However, the insensitivity of the steady-state inactivation to changes in

the extracellular divalent cation concentration is a more challenging puzzle to unravel.

It has been demonstrated that the voltage-dependent parameters of voltage-gated ion channels are responsive to an elevation of extracellular cation concentration (see Neumaier et al., 2015 for review). According to the Gouy-Chapman-Stern model, fixed negative charges present at the surface of the membrane and/or the channel create a local negative surface potential that is reduced by increasing extracellular divalent cations, resulting in a positive shift of the voltage-dependent parameters (Hille, 1992a; Gilbert and Ehrenstein, 1969; Neumaier et al., 2015). In this theoretical framework, the four voltage-sensing domains (VSD) of a channel should be affected, i.e., all the voltage-dependent parameters, including the voltage-dependence of activation and inactivation, should be sensitive to the changes in the surface potential. In  $\text{Na}_v$  and  $\text{Ca}_v$  channels, this prediction is validated (see Table 3). In  $\text{Ca}_v4$ , both voltage dependency and kinetics of inactivation should be under the control of at least the IFM motif and the S4 helices of domain III and/or IV (Capes et al., 2013; Angsutararux et al., 2021). The observation that only inactivation is not influenced by this surface charges screening strongly suggests a highly localized effect on the S4 of domains III and/or IV (Capes et al., 2013; Angsutararux et al., 2021; Lewis and Raman, 2013). This effect is not observed with  $\text{Na}_v$  or  $\text{Ca}_v$  channels (see Fig. 5) (Neumaier et al., 2015). Interestingly, the S4 helices of domains III and IV of  $\text{Ca}_v4$  exhibit a high degree of conservation with those of  $\text{Na}_v$  or

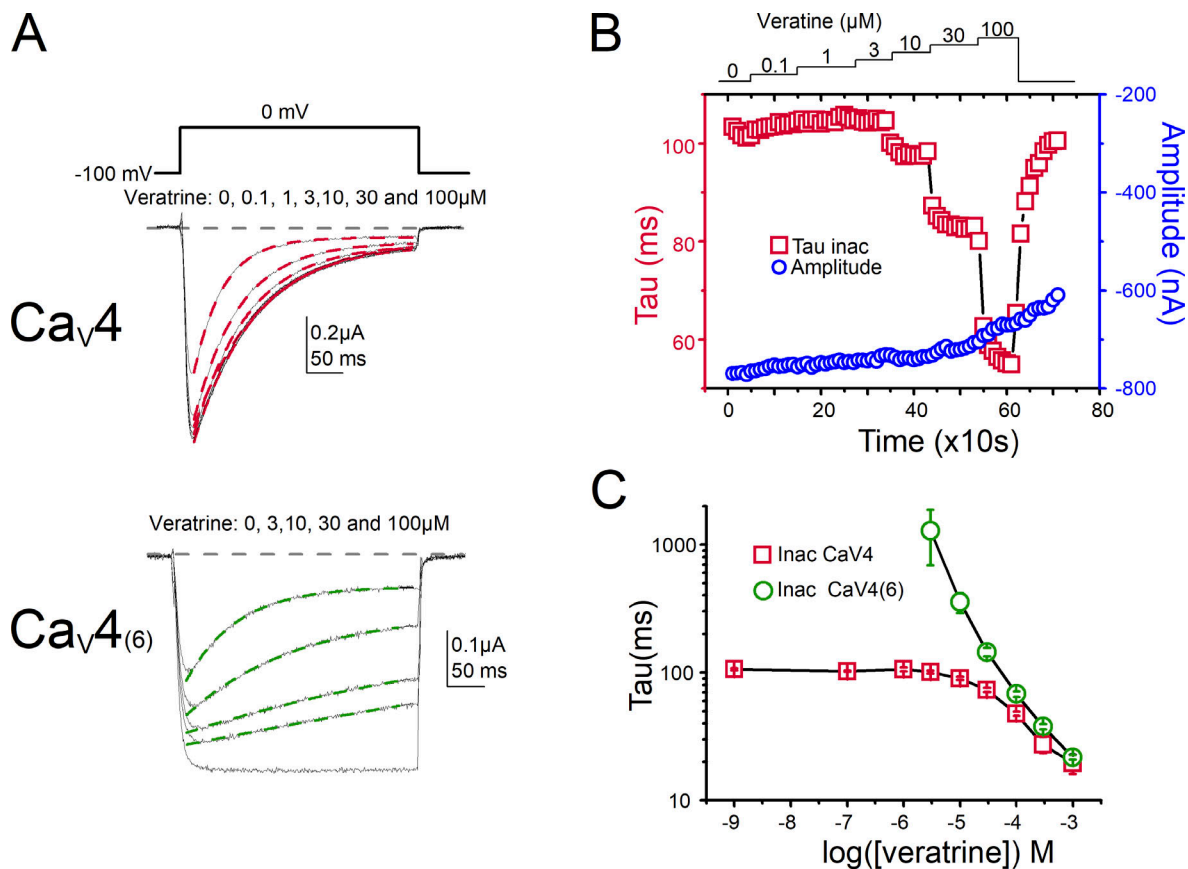


Figure 11. **Effect of veratrine (30  $\mu\text{M}$ ) on  $\text{Ca}_v4$  current amplitude and inactivation.** (A) Exemplar current traces of *Xenopus* oocytes expressing the  $\text{Ca}_v4$  or the mutated  $\text{Ca}_v4(6)$  channel in control  $\text{Ba}^{2+}$  conditions (in black), and at the steady-state effect of the perfusion of different concentrations of veratrine (in red, the fit of inactivation using a single exponential, values are given in C). (B) Time course of the effects of different concentrations of veratrine (values are given at the top of the figure) on the current amplitude (blue circle) and on current inactivation quantified using a single exponential fit ( $\tau$ , red square). (C) Graph showing the values of the exponential fit of inactivation at the steady state level of each concentration for the wild-type  $\text{Ca}_v4$  (red square) and the mutant  $\text{Ca}_v4(6)$  (green circle), as a function of veratrine concentrations. Note that for high doses, the inactivation of the mutant is almost equal to that of the wild type, despite the lack of MFL-driven inactivation.

$\text{Ca}_v$  channels, featuring the same number of positive charges at similar positions.

Alternatively, alteration of either the interactions of the S4s with other channel helices during gating or modifications of the fixed charges at the surface of the channels both in terms of their quantity and arrangement may be questioned instead of focusing solely on S4 itself. Indeed, interactions involving voltage-sensor in domains III and IV, with residues surrounding pore sequence (S4-S5 linkers in domains III and IV and the III-IV loop, S3 helices negative charges), are known to modulate both voltage dependence and kinetics of activation, and inactivation in  $\text{Na}_v$  and  $\text{Ca}_v$  channels (Fernández-Quintero et al., 2021; Lewis and Raman, 2013; Capes et al., 2013; Angsutararux et al., 2021; Hsu et al., 2017). These interactions could potentially be responsible for the fact that the potential for half-activation and inactivation of  $\text{Ca}_v4$  are more hyperpolarized compared with other mammalian  $\text{Ca}_v$  channels such as  $\text{Ca}_v2.1$  or  $\text{Ca}_v1.2$ , see Tables 1 and 2), and depolarized when compared with the  $\text{Na}_v$  channels. However, whether they can modulate the sensing of a local electric field by the S4, or the properties of this field as referred to the existence of the surface potential, is not

known and will require additional experimental work to be understood.

This insensitivity may also be related to modification of the electrostatic surface potential in the surrounding of these two voltage-sensors either by a modification in the number of the charges at their surface or a change in the affinity of these surface charges to divalent cations (Elinder et al., 1996; Madeja, 2000) producing either saturation at low concentration or insensitivity to binding. The number and position of the negative or positive charges in the S3-S4 segment of  $\text{Na}_v1.5$ ,  $\text{Ca}_v4$ , or  $\text{Ca}_v1.2$  for example are different. However, the precise molecular structure of  $\text{Ca}_v4$  is not known. Calculating the real surface potential locally, in the vicinity of these VSDs is therefore highly challenging and speculative. Finally, one cannot exclude the possibility of similar electrostatic surface potential to other channels partially, or totally, counterbalanced by a direct effect of the incoming  $\text{Ca}^{2+}$  ion on the VDI. In  $\text{Ca}_v1.2$  channel, it has been demonstrated, for example, that mutation of a single aspartate residue in the selectivity filter of  $\text{Ca}_v1.2$  (D707 at position +1, after the conserved E of domain II) can remove CDI without any other effect on the channel properties (Abderemane-Ali

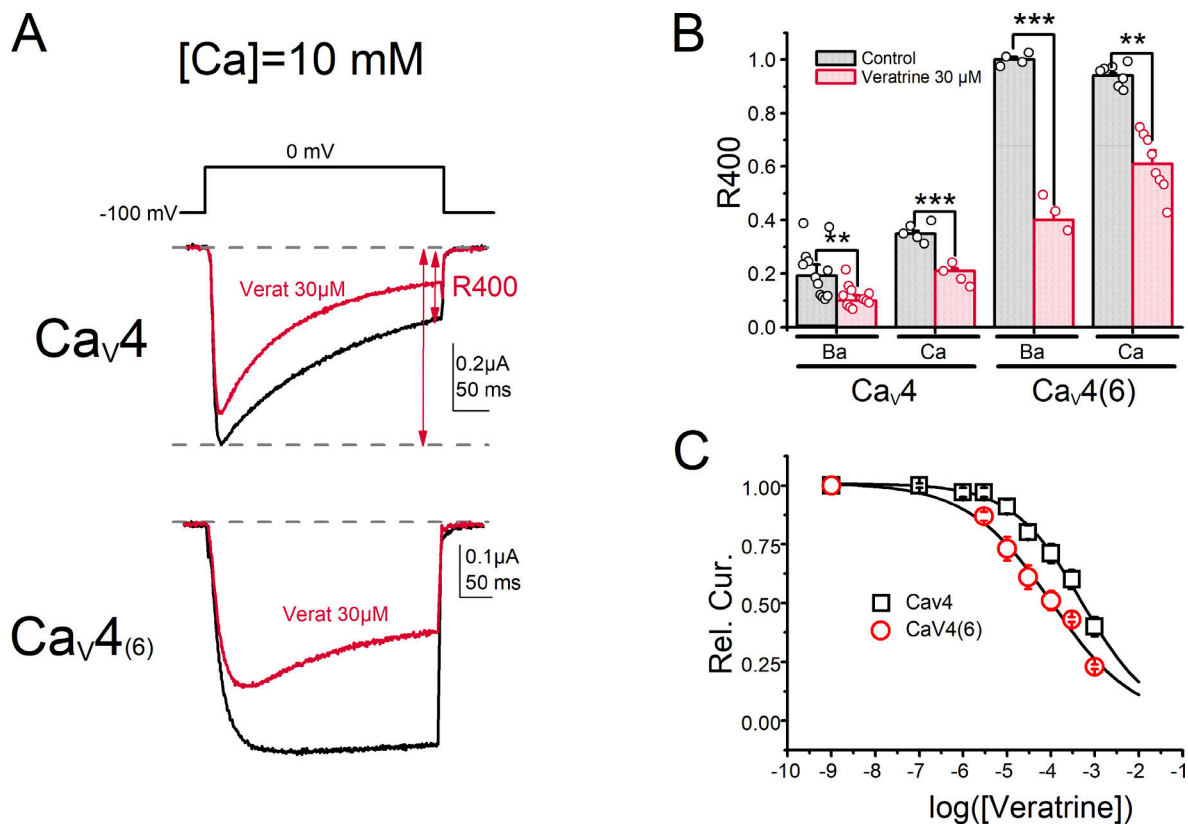


**Figure 12. Effects of veratrine (30  $\mu$ M) on Ca<sub>V</sub>4 in Ca<sup>2+</sup>-containing solution.** (A) Current traces were recorded during 400 s pulses from  $-100$  to  $0$  mV on *Xenopus* oocytes expressing Ca<sub>V</sub>4 (top) or Ca<sub>V</sub>4(6) (bottom), in the control condition (black traces) or at the steady-state effect of veratrine (red traces). R400 is the ratio of the peak current amplitude over the current amplitude measured at the end of the stimulation pulse. (B) Histogram showing the R400 values calculated for Ca<sub>V</sub>4 or Ca<sub>V</sub>4(6) current traces recorded in Ba<sup>2+</sup> or in Ca<sup>2+</sup> without (black bars) or with veratrine (red bars). Mann-Whitney rank sum test,  $P = 0.004$ ; Student's  $t$  test,  $P = 0.00003$  and  $8.3 \times 10^{-7}$ ; and Mann-Whitney rank sum test,  $P = 0.002$ , respectively. (C) Dose-response curves of veratrine on the peak current amplitudes recorded on *Xenopus* oocytes expressing Ca<sub>V</sub>4 or Ca<sub>V</sub>4 (6) (holding potential  $-100$  mV, step depolarization to  $0$  mV).

et al., 2019), demonstrating the role of intrapore cation-binding site on inactivation. Unfortunately, studies looking at the effect of the divalent cations on the role of these DIII-DIV voltage sensors are lacking. The molecular mechanism of CatDI will therefore require additional experiments to be fully explained.

#### Ca<sub>V</sub>4 channel CatDI versus Ca<sub>V</sub>1.2 CDI

Another surprising observation is the slowing of inactivation when Ca<sup>2+</sup> is the charge carrier (called here CatDI). The CDI of Ca<sub>V</sub> channels has been well described (Budde et al., 2002; Ben-Johny et al., 2014), and produces, on mammalian Ca<sub>V</sub>1 or Ca<sub>V</sub>2 channels, faster inactivation kinetics. In fact, in Ca<sub>V</sub>1 or Ca<sub>V</sub>2 channels, this Ca dependency appears to be more a Ca<sup>2+</sup> calmodulin-dependent regulation of the classical voltage-dependent inactivation rather than a completely distinct mechanism (Cens et al., 1999; De Leon et al., 1995; Budde et al., 2002). Calmodulin bound to the Ca<sub>V</sub>1.2 C-terminal tail constitutes the Ca-sensing element able to detect, very locally, incoming Ca<sup>2+</sup> ions during channel opening and to trigger channel CDI. An EF-hand structure is also important for this process, although it is proposed not to be able to bind Ca<sup>2+</sup> ions, but rather to play a role in CaM binding (Gardill et al., 2019). The displacement of CaM from one binding site to another on the channel may allow or

accelerate a pre-existing voltage-dependent inactivation, thus producing the so-called CDI (Cens et al., 1999, 2006; De Leon et al., 1995; Budde et al., 2002). In Na<sub>V</sub> channels, while these Ca<sup>2+</sup>/CaM binding structures (IQ and EF-hand sequences) are also present on the C-terminal tail and the III–IV loop (Salvage et al., 2021), the Ca<sup>2+</sup>-dependent regulation of gating is translated by a decrease in the peak current and/or a shift in the inactivation curve, depending on the expressed Na<sub>V</sub> channels (Pitt and Lee, 2016; Salvage et al., 2021; Ben-Johny et al., 2014). In contrast, a clear effect on the inactivation kinetics has rarely been described, probably due to the lack of Ca<sup>2+</sup> permeability of the Na<sub>V</sub> channel. These regulations have thus been analyzed by varying the bulk intracellular Ca<sup>2+</sup> concentration, which also induced activation of intracellular regulatory pathways (CaM kinase, PKC...). This is not the case for Ca<sub>V</sub>4, for which the slowing of inactivation by Ca<sup>2+</sup> occurs in  $<2$ – $5$  s (see Fig. 1), which strongly suggests a direct effect of Ca<sup>2+</sup> on Ca<sub>V</sub>4. While this slowing clearly requires an inward flux of Ca<sup>2+</sup>, since it is not seen on outward current (Fig. 6), it does not have the hallmark of CDI, i.e., it is not proportional to the amplitude of the Ca<sup>2+</sup> influx (see Fig. 4 D), and, as opposed to the classical CDI, CaM does not seem to be involved (Ben-Johny and Yue, 2014; Peterson et al., 1999). Loss of CatDI with the Ca<sub>V</sub>4(8) chimera suggests, however, that the C-terminal tail, in one way or another, may be involved. We



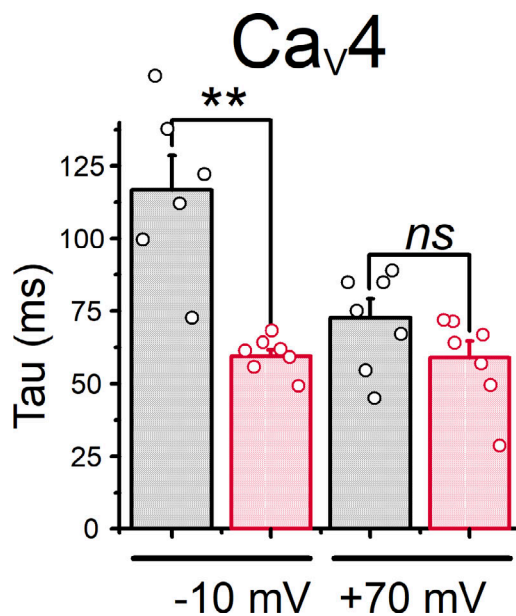


Figure 13. **Effect of veratrine (50  $\mu$ M) on  $\text{Ca}_v4$  channels at positive voltages.** Inactivation time constants measured for  $\text{Ba}^{2+}$  current recorded on *Xenopus* oocytes expressing  $\text{Ca}_v4$  without (in black) or with 50  $\mu$ M veratrine (in red) either 0 or +70 mV. Only at -10 mV are these differences statistically significant: Mann-Whitney rank sum test, P values are 0.002 and 0.057, respectively.

conclude that CatDI is clearly different from CDI. The aspartate at position +1 relative to SF in domains II (D707), crucial for  $\text{Ca}_v1.2$  CDI (Abderemane-Ali et al., 2019), is conserved in all mammalian  $\text{Ca}_v$  channels but not in  $\text{Na}_v$  or  $\text{Ca}_v4$ . The role of this substitution in the lack of CDI in  $\text{Ca}_v4$ , harboring CaM, CaM-binding sites, and the EF-hand motif in their sequence needs to be further studied. Interestingly, still in  $\text{Ca}_v1.2$ , mutation of the glutamate in the SF of domain III has the same effect as D707 and completely suppresses CDI. In  $\text{Ca}_v4$ , the glutamate at the SF of domain III is conserved, but not that of the SF at domain IV. Alteration of this  $\text{Ca}^{2+}$  binding site within the  $\text{Ca}_v4$  SF could therefore drive the change not only in the cationic channel selectivity, as suggested earlier, but also in the  $\text{Ca}^{2+}$  dependence of the inactivation mechanism. Mutagenesis experiments are in progress to explore this possibility. All of these properties make  $\text{Ca}_v4$  CatDI a novel mechanism regulating  $\text{Ca}^{2+}$  influx.

#### $\text{Ca}_v4$ channel pharmacology

$\text{Ca}_v4$  insensitivity to neonicotinoids and phenyl insecticides is not surprising. However, due to the amino acid sequence similarity with the  $\text{Na}_v$  channel, a potential susceptibility to pyrethroids could be expected. This was not the case either, and a close examination of the amino acids reveals that key positions for knockdown resistance in *Drosophila*  $\text{Na}_v$  channels (specifically in S3-S4 DII [M918], S6 DII [L1011], and S6 DIII [F1534]; Rinkevich et al., 2013) are occupied by amino acids that confer resistance (I1202, M1297, and C1830, respectively) in  $\text{Ca}_v4$ .

The only molecules that were active on the  $\text{Ca}_v4$  channels were a  $\text{Ca}_v1$  channel antagonist, diltiazem (which decreases current amplitude), and a  $\text{Na}_v$  channel regulator, veratrine

(which accelerates inactivation kinetics; see Figs. 7 and 8). The amino acids that have been shown to be implicated in diltiazem binding within the pore of the  $\text{Ca}_v1.1$  channel (Zhao et al., 2019) and implicated in the effects on current amplitude (Tyr1365, Ala1369, and Ile1372 of S6DI [Hering et al., 1996]) are not conserved in  $\text{Ca}_v4$ , although the inhibition of the peak current is similar. In the  $\text{Ca}_v4$  channel, the benzothiazepines binding site is therefore not completely conserved. We are currently working on pinpointing the channel's susceptibility to diltiazem, and identifying the specific amino acids involved in these binding sites.

The effect of veratrine is unexpected: it leads to an acceleration of the inactivation kinetics on  $\text{Ca}_v4$ , which contrasts with its opposite effect recorded on  $\text{Na}_v$  channels, where it slows the inactivation and deactivation kinetics. Interestingly, this acceleration is also observed with the mutant that lacks inactivation, ( $\text{Ca}_v4(6)$ , Fig. 11), and both processes seem to converge toward similar values (Fig. 11 C). Veratridine, the major component of veratrine has similar effects on  $\text{Ca}_v4$ , but slows honeybee  $\text{Na}_v$  channel inactivation and deactivation. On the mammalian  $\text{Na}_v1.5$  channel, two binding sites for veratridine have been proposed: (1) in the pore at the level of the SF, and (2) at the intracellular mouth of the pore, at the bottom of the S6 (Gulsevian et al., 2022). A mutagenesis analysis revealed that the most probable binding site is site 2, in which amino acids L409, E417, and I1466 would be the most important for the stabilization of the ligand. These amino acids are conserved at homologous positions in  $\text{Ca}_v4$ , and molecular docking of veratrine on an alpha-fold model of  $\text{Ca}_v4$  shows poses of the molecule at this site (not shown), suggesting that the same or very close binding sites on  $\text{Na}_v1.5$  and  $\text{Ca}_v4$  can produce opposite effects, as already seen for the  $\text{Ca}_v1.2$   $\text{Ca}^{2+}$  channel and dihydropyridines (Zhao et al., 2019). Amino acids at equivalent positions in domains I, II, III, and IV of  $\text{Na}_v$ ,  $\text{Ca}_v$  channels, or subunits of Kv channels have been shown to be central for the formation of the activation gate and for the development of fast and slow C-type inactivation (Shi and Soldatov, 2002; Chancey et al., 2007; Liu et al., 2023). The fact that the  $\text{Ca}_v4(6)$  mutant, which lacks inactivation, is also sensitive to veratrine with the same functional effects has led us to conclude that this acceleration of inactivation does not depend on the MFL motif but requires another molecular mechanism. One may speculate that upon binding at the bottom of one or multiple S6 segments, veratrine could induce a structural rearrangement of the pore and/or the SF and produce an acceleration of inactivation via a process similar to the C-type inactivation that is present in most voltage-gated ion channel types and has been attributed to a restructuring (either constriction or dilatation) of the selectivity filter inducing non-conductivity, and thus inactivation (Reddi et al., 2022; Cuello et al., 2010; Pavlov et al., 2005; Irie et al., 2010). In potassium channels, different mutations within the selectivity filter or at the internal mouth of the channel (specifically at the bottom of the S6 segment) have been demonstrated to impact the C-type inactivation (Li et al., 2021; Cuello et al., 2010; Tan et al., 2022; Reddi et al., 2022). Furthermore, although infrequent, there is precedent for the regulatory effects of certain drugs or ions on C-type inactivation (Armstrong and Hoshi, 2014; Chen et al.,

2013). In this context, the fact that the inactivation time constant is independent of the voltage but dependent upon the direction of the permeating ion (see Fig. 10 B) could possibly be explained by the differential stabilization of the pore structure by divalent cation binding at the extracellular ion binding site during inward but not outward currents. Alternatively, an open-channel block can also be a possible mechanism. The single-channel signatures of these two processes might be different, and this eventuality is now being evaluated at the single-channel level. In any case, in the absence of other specific inhibitors, the use of veratrine may constitute a very useful tool to identify the expression of  $Ca_v4$  in living insect tissues, but it may also possibly help, through structural studies, to shed new light on the C-type channel inactivation mechanism and regulation.

In conclusion, this study has revealed several distinctive properties of the  $Ca_v4$  channel, including (1) its exclusive permeability to calcium, (2) insensitivity of the voltage-dependent inactivation to surface potential, (3) a specific type of CatDI, and (4) a pharmacological profile divergent from  $Na_v$  and  $Ca_v$  channels. These unique features unequivocally define a novel type of voltage-gated  $Ca^{2+}$  channels specific to insects, establishing a new phylogenetic and functional connection between  $Na_v$  and  $Ca_v$ . The identified characteristics demand further comprehensive analysis and are poised to offer invaluable insights into the functional molecular mechanisms not only of  $Ca_v4$  but also of  $Na_v$  and other  $Ca_v$  channels. It should be noted, however, that purified  $Ca_v4$  channels from native insect tissues have not yet been obtained. Therefore, the biophysical and pharmacological properties of this channel in vivo may differ significantly from those described here if regulatory subunits exist, as described for other voltage-gated Ca, Na, or K channels.

### Data availability

The data are directly available from the corresponding author upon reasonable request by email.

## Acknowledgments

Christopher J. Lingle served as editor.

A special thanks to Mécédès Charreton (INRAE), Sylvain Roque (Centre National de la Recherche Scientifique), and Karine Allenne (University of Montpellier) for their invaluable help in honeybee and *Xenopus* preparation and administrative work.

The authors would like to acknowledge the Centre National de la Recherche Scientifique (CNRS), the Institut National de la Santé et de la Recherche Médicale (INSERM), l'Institut national de Recherche pour l'Agriculture, l'Alimentation et l'Environnement (INRAE), and the Agence National pour la Recherche (ANR Synaptic-Bee: ANR-20-CE34-0017-01) for financial support. We acknowledge the support of the Natural Sciences and Engineering Research Council of Canada (NSERC) Discovery Grant (RGPIN-2020-06359) and NSERC Alliance International Catalyst grant (572132-2022) to Mohamed Chahine.

Author contributions: Investigation: A. Bertaud, T. Cens, M. Rousset, L. Soussi, A. Kadala, C. Collet, P. Gosselin-Badaroudine, J. Roussel, M. Chahine, and P. Charnet. Conceptualization: T. Cens, P. Bois, M. Chahine, and P. Charnet. Formal analysis: T.

Cens, P. Gosselin-Badaroudine, and P. Charnet. Methodology: T. Cens, C. Ménard, A. Chavanieu, C. Collet, and P. Charnet. Writing - review & editing: T. Cens, C. Collet, P. Bois, J.-B. Thibaud, M. Vignes, M. Chahine, and P. Charnet. Data curation for molecular structure: A. Chavanieu, S. Esteran, M. Chahine, and P. Charnet. Validation: J.-B. Thibaud, M. Chahine, and P. Charnet. Resources: S. Dutertre and P. Charnet. Funding acquisition: M. Chahine and P. Charnet. Project administration: P. Charnet. Writing - original draft: P. Charnet.

Disclosures: The authors declare no competing interests exist.

Submitted: 27 November 2023

Revised: 2 February 2024

Revised: 5 March 2024

Accepted: 12 March 2024

## References

- Abderemane-Ali, F., F. Findeisen, N.D. Rossen, and D.L. Minor Jr. 2019. A selectivity filter gate controls voltage-gated calcium channel calcium-dependent inactivation. *Neuron*. 101:1134–1149.e3. <https://doi.org/10.1016/j.neuron.2019.01.011>
- Angsutararux, P., P.W. Kang, W. Zhu, and J.R. Silva. 2021. Conformations of voltage-sensing domain III differentially define  $Na_v$  channel closed- and open-state inactivation. *J. Gen. Physiol.* 153:e202112891. <https://doi.org/10.1085/jgp.202112891>
- Armstrong, C.M., and T. Hoshi. 2014.  $K^+$  channel gating: C-Type inactivation is enhanced by calcium or lanthanum outside. *J. Gen. Physiol.* 144: 221–230. <https://doi.org/10.1085/jgp.201411223>
- Ben-Johny, M., P.S. Yang, J. Niu, W. Yang, R. Joshi-Mukherjee, and D.T. Yue. 2014. Conservation of  $Ca^{2+}$ /calmodulin regulation across Na and  $Ca^{2+}$  channels. *Cell*. 157:1657–1670. <https://doi.org/10.1016/j.cell.2014.04.035>
- Ben-Johny, M., and D.T. Yue. 2014. Calmodulin regulation (calmodulation) of voltage-gated calcium channels. *J. Gen. Physiol.* 143:679–692. <https://doi.org/10.1085/jgp.201311153>
- Brunello, L., C. Ménard, M. Rousset, M. Vignes, P. Charnet, and T. Cens. 2022. Different efficiency of auxiliary/chaperone proteins to promote the functional reconstitution of honeybee glutamate and acetylcholine receptors in *Xenopus laevis* oocytes. *Insect Mol. Biol.* 31:620–633. <https://doi.org/10.1111/imb.12791>
- Budde, T., S. Meuth, and H.-C. Pape. 2002. Calcium-dependent inactivation of neuronal calcium channels. *Nat. Rev. Neurosci.* 3:873–883. <https://doi.org/10.1038/nrn959>
- Capes, D.L., M.P. Goldschen-Ohm, M. Arcisio-Miranda, F. Bezanilla, and B. Chanda. 2013. Domain IV voltage-sensor movement is both sufficient and rate limiting for fast inactivation in sodium channels. *J. Gen. Physiol.* 142:101–112. <https://doi.org/10.1085/jgp.201310998>
- Castella, C., M. Amichot, J.B. Bergé, and D. Pauron. 2001. DSC1 channels are expressed in both the central and the peripheral nervous system of adult *Drosophila melanogaster*. *Invert. Neurosci.* 4:85–94. <https://doi.org/10.1007/s101580100010>
- Catterall, W.A. 2000. Structure and regulation of voltage-gated  $Ca^{2+}$  channels. *Annu. Rev. Cell Dev. Biol.* 16:521–555. <https://doi.org/10.1146/annurev.cellbio.16.1.521>
- Catterall, W.A. 2013. Voltage-gated sodium channels at 60: Structure, function, and pathophysiology. *J. Physiol.* 590:2577–2589. <https://doi.org/10.1113/jphysiol.2011.224204>
- Cens, T., S. Restituito, S. Galas, and P. Charnet. 1999. Voltage and calcium use the same molecular determinants to inactivate calcium channels. *J. Biol. Chem.* 274:5483–5490. <https://doi.org/10.1074/jbc.274.9.5483>
- Cens, T., M. Rousset, C. Collet, M. Charreton, L. Garnery, Y. Le Conte, M. Chahine, J.C. Sandoz, and P. Charnet. 2015. Molecular characterization and functional expression of the *Apis mellifera* voltage-dependent  $Ca^{2+}$  channels. *Insect Biochem.* 58:12–27. <https://doi.org/10.1016/j.ibmb.2015.01.005>
- Cens, T., M. Rousset, C. Collet, V. Raymond, F. Démares, A. Quintavalle, M. Bellis, Y. Le Conte, M. Chahine, and P. Charnet. 2013. Characterization of the first honeybee  $Ca^{2+}$  channel subunit reveals two novel species-

- and splicing-specific modes of regulation of channel inactivation. *Pflügers Arch.* 465:985–996. <https://doi.org/10.1007/s00424-013-1223-2>
- Cens, T., M. Rousset, A. Kajava, and P. Charnet. 2007. Molecular determinant for specific Ca/Ba selectivity profiles of low and high threshold Ca<sup>2+</sup> channels. *J. Gen. Physiol.* 130:415–425. <https://doi.org/10.1085/jgp.200709771>
- Cens, T., M. Rousset, J.P. Leyris, P. Fesquet, and P. Charnet. 2006. Voltage- and calcium-dependent inactivation in high voltage-gated Ca(2+) channels. *Prog. Biophys. Mol. Biol.* 90:104–117. <https://doi.org/10.1016/j.pbiomolbio.2005.05.013>
- Chancey, J.H., P.E. Shockett, and J.P. O'Reilly. 2007. Relative resistance to slow inactivation of human cardiac Na<sup>+</sup> channel hNav1.5 is reversed by lysine or glutamine substitution at V930 in D2-S6. *Am. J. Physiol. Cell Physiol.* 293:C1895–C1905. <https://doi.org/10.1152/ajpcell.00377.2007>
- Chen-Lzu, Y., R.M. Shaw, G.S. Pitt, V. Yarov-Yarovoy, J.T. Sack, H. Abriel, R.W. Aldrich, L. Belardinelli, M.B. Cannell, W.A. Catterall, et al. 2015. Na<sup>+</sup> channel function, regulation, structure, trafficking and sequestration. *J. Physiol.* 593:1347–1360. <https://doi.org/10.1113/jphysiol.2014.281428>
- Chen, H., D. Zhang, J. Hua Ren, and S. Ping Chao. 2013. Effects of L-type calcium channel antagonists verapamil and diltiazem on fKv1.4ΔN Currents in *Xenopus oocytes*. *Iran. J. Pharm. Res.* 12:855–866.
- Chen, X., Y. Wang, W. Wu, K. Dong, and Z. Hu. 2018. DSC1 channel-dependent developmental regulation of pyrethroid susceptibility in *Drosophila melanogaster*. *Pestic. Biochem. Physiol.* 148:190–198. <https://doi.org/10.1016/j.pestbp.2018.04.014>
- Cibulsky, S.M., and W.A. Sather. 2000. The EEEE locus is the sole high-affinity Ca(2+) binding structure in the pore of a voltage-gated Ca(2+) channel: Block by Ca(2+) entering from the intracellular pore entrance. *J. Gen. Physiol.* 116:349–362. <https://doi.org/10.1085/jgp.116.3.349>
- Collet, C., A. Kadala, B. Vaissière, M. Rousset, T. Cens, Y. Le Conte, M. Chahine, J.B. Thibaud, and P. Charnet. 2016. Differential action of pyrethroids on honey bee and bumble bee voltage-gated sodium channels. *Biophys. J.* 110:112a. <https://doi.org/10.1016/j.bpj.2015.11.660>
- Cuello, L.G., V. Jogini, D.M. Cortes, and E. Perozo. 2010. Structural mechanism of C-type inactivation in K(+) channels. *Nature.* 466:203–208. <https://doi.org/10.1038/nature09153>
- Cui, Y.-J., L.-L. Yu, H.-J. Xu, K. Dong, and C.-X. Zhang. 2012. Molecular characterization of DSC1 orthologs in invertebrate species. *Insect Biochem. Mol. Biol.* 42:353–359. <https://doi.org/10.1016/j.ibmb.2012.01.005>
- Dong, K., Y. Du, F. Rinkevich, Y. Nomura, P. Xu, L. Wang, K. Silver, and B.S. Zhorov. 2014. Molecular biology of insect sodium channels and pyrethroid resistance. *Insect Biochem. Mol. Biol.* 50:1–17. <https://doi.org/10.1016/j.ibmb.2014.03.012>
- Dong, K., Y. Du, F. Rinkevich, L. Wang, and P. Xu. 2015. The *Drosophila* Sodium Channel 1 (DSC1): The founding member of a new family of voltage-gated cation channels. *Pestic. Biochem. Physiol.* 120:36–39. <https://doi.org/10.1016/j.pestbp.2014.12.005>
- Dudev, T., and C. Lim. 2014a. Ion selectivity strategies of sodium channel selectivity filters. *Acc. Chem. Res.* 47:3580–3587. <https://doi.org/10.1021/ar5002878>
- Dudev, T., and C. Lim. 2014b. Evolution of eukaryotic ion channels: Principles underlying the conversion of Ca<sup>2+</sup>-selective to Na<sup>+</sup>-selective channels. *J. Am. Chem. Soc.* 136:3553–3559. <https://doi.org/10.1021/ja4121132>
- Elinder, F., M. Madeja, and P. Arhem. 1996. Surface charges of K channels. Effects of strontium on five cloned channels expressed in *Xenopus oocytes*. *J. Gen. Physiol.* 108:325–332. <https://doi.org/10.1085/jgp.108.4.325>
- Fernández-Quintero, M.L., Y. El Ghaleb, P. Tuluc, M. Campiglio, K.R. Liedl, and B.E. Flucher. 2021. Structural determinants of voltage-gating properties in calcium channels. *Elife.* 10:e64087. <https://doi.org/10.7554/eLife.64087>
- Fux, J.E., A. Mehta, J. Moffat, and J.D. Spafford. 2018. Eukaryotic voltage-gated sodium channels: On their origins, asymmetries, losses, diversification and adaptations. *Front. Physiol.* 9:1406. <https://doi.org/10.3389/fphys.2018.01406>
- Gardill, B.R., R.E. Rivera-Acevedo, C.-C.C. Tung, and F. Van Petegem. 2019. Crystal structures of Ca<sup>2+</sup>-calmodulin bound to Nav C-terminal regions suggest role for EF-hand domain in binding and inactivation. *Proc. Natl. Acad. Sci. USA.* 116:10763–10772. <https://doi.org/10.1073/pnas.1818618116>
- Gilbert, D.L., and G. Ehrenstein. 1969. Effect of divalent cations on potassium conductance of squid axons: Determination of surface charge. *Biophys. J.* 9:447–463. [https://doi.org/10.1016/S0006-3495\(69\)86396-4](https://doi.org/10.1016/S0006-3495(69)86396-4)
- Gosselin-Badaroudine, P., P. Charnet, C. Collet, and M. Chahine. 2017. Met-aflumizone inhibits the honeybee Nav<sub>1</sub> channel by targeting recovery from slow inactivation. *FEBS Lett.* 591:3842–3849. <https://doi.org/10.1002/1873-3468.12897>
- Gosselin-Badaroudine, P., A. Moreau, L. Delemotte, T. Cens, C. Collet, M. Rousset, P. Charnet, M.L. Klein, and M. Chahine. 2015. Characterization of the honeybee AmNav1 channel and tools to assess the toxicity of insecticides. *Sci. Rep.* 5:12475. <https://doi.org/10.1038/srep12475>
- Gosselin-Badaroudine, P., A. Moreau, L. Simard, T. Cens, M. Rousset, C. Collet, P. Charnet, and M. Chahine. 2016. Biophysical characterization of the honeybee DSC1 orthologue reveals a novel voltage-dependent Ca<sup>2+</sup> channel subfamily: Cav4. *J. Gen. Physiol.* 148:133–145. <https://doi.org/10.1085/jgp.201611614>
- Guia, A., M.D. Stern, E.G. Lakatta, and I.R. Josephson. 2001. Ion concentration-dependence of rat cardiac unitary L-type calcium channel conductance. *Biophys. J.* 80:2742–2750. [https://doi.org/10.1016/S0006-3495\(01\)76242-X](https://doi.org/10.1016/S0006-3495(01)76242-X)
- Gulsevin, A., A.M. Glazer, T. Shields, B.M. Kroncke, D.M. Roden, and J. Meiler. 2022. Veratridine can bind to a site at the mouth of the channel pore at human cardiac sodium channel Nav1.5. *Int. J. Mol. Sci.* 23:2225–2238. <https://doi.org/10.3390/ijms23042225>
- Gur Barzilai, M., A.M. Reitzel, J.E.M. Kraus, D. Gordon, U. Technau, M. Gurevitz, and Y. Moran. 2012. Convergent evolution of sodium ion selectivity in metazoan neuronal signaling. *Cell Rep.* 2:242–248. <https://doi.org/10.1016/j.celrep.2012.06.016>
- Heinemann, S.H., H. Terlau, W. Stühmer, K. Imoto, S. Numa, W. Stühmer, K. Imoto, and S. Numa. 1992. Calcium channel characteristics conferred on the sodium channel by single mutations. *Nature.* 356:441–443. <https://doi.org/10.1038/356441a0>
- Hering, S., S. Aczél, M. Grabner, F. Döring, S. Berjukow, J. Mitterdorfer, M.J. Sinnegger, J. Striessnig, V.E. Degtiar, Z. Wang, and H. Glossmann. 1996. Transfer of high sensitivity for benzothiazepines from L-type to class A (BI) calcium channels. *J. Biol. Chem.* 271:24471–24475. <https://doi.org/10.1074/jbc.271.40.24471>
- Hille, B. 1992a. Ion channels of Excitable Membranes. Third edition. Oxford University Press, Oxford, UK.
- Hille, B. 1992b. Ionic channels of Excitable Membranes. Second edition. Oxford University Press, Oxford, UK.
- Hong, C.S., and B. Ganetzky. 1994. Spatial and temporal expression patterns of two sodium channel genes in *Drosophila*. *J. Neurosci.* 14:5160–5169. <https://doi.org/10.1523/JNEUROSCI.14-09-05160.1994>
- Hsu, E.J., W. Zhu, A.R. Schubert, T. Voelker, Z. Varga, and J.R. Silva. 2017. Regulation of Na<sup>+</sup> channel inactivation by the DIII and DIV voltage-sensing domains. *J. Gen. Physiol.* 149:389–403. <https://doi.org/10.1085/jgp.201611678>
- Irie, K., K. Kitagawa, H. Nagura, T. Imai, T. Shimomura, and Y. Fujiyoshi. 2010. Comparative study of the gating motif and C-type inactivation in prokaryotic voltage-gated sodium channels. *J. Biol. Chem.* 285:3685–3694. <https://doi.org/10.1074/jbc.M109.057455>
- Jiang, D., H. Shi, L. Tonggu, T.M. Gamal El-Din, M.J. Lenaeus, Y. Zhao, C. Yoshioka, N. Zheng, and W.A. Catterall. 2020. Structure of the cardiac sodium channel. *Cell.* 180:122–134.e10. <https://doi.org/10.1016/j.cell.2019.11.041>
- Johnson, C.N. 2020. Calcium modulation of cardiac sodium channels. *J. Physiol.* 598:2835–2846. <https://doi.org/10.1113/JP277553>
- Kontis, K.J., A. Rounaghi, and A.L. Goldin. 1997. Sodium channel activation gating is affected by substitutions of voltage sensor positive charges in all four domains. *J. Gen. Physiol.* 110:391–401. <https://doi.org/10.1085/jgp.110.4.391>
- Kulkarni, N.H., A.H. Yamamoto, K.O. Robinson, T.F.C. Mackay, and R.R.H. Anholt. 2002. The DSC1 channel, encoded by the smi60E locus, contributes to odor-guided behavior in *Drosophila melanogaster*. *Genetics.* 161:1507–1516. <https://doi.org/10.1093/genetics/161.4.1507>
- De Leon, M., Y. Wang, L. Jones, E. Perez-Reyes, X. Wei, T.W. Soong, T.P. Snutch, and D.T. Yue. 1995. Essential Ca<sup>2+</sup>-binding motif for Ca<sup>2+</sup>-sensitive inactivation of L-type Ca<sup>2+</sup> channels. *Science.* 270:1502–1506. <https://doi.org/10.1126/science.270.5241.1502>
- Lewis, A.H., and I.M. Raman. 2013. Interactions among DIV voltage-sensor movement, fast inactivation, and resurgent Na current induced by the Navβ4 open-channel blocking peptide. *J. Gen. Physiol.* 142:191–206. <https://doi.org/10.1085/jgp.201310984>
- Li, J., R. Shen, B. Reddy, E. Perozo, and B. Roux. 2021. Mechanism of C-type inactivation in the hERG potassium channel. *Sci. Adv.* 7:1–8. <https://doi.org/10.1126/sciadv.abd6203>
- Liu, Y., C.A.Z. Bassetto Jr., B.I. Pinto, and F. Bezanilla. 2023. A mechanistic reinterpretation of fast inactivation in voltage-gated Na<sup>+</sup> channels. *Nat. Commun.* 14:5072. <https://doi.org/10.1038/s41467-023-40514-4>
- Liu, Z., I. Chung, and K. Dong. 2001. Alternative splicing of the BSC1 gene generates tissue-specific isoforms in the German cockroach. *Insect Biochem. Mol. Biol.* 31:703–713. [https://doi.org/10.1016/S0965-1748\(00\)00178-8](https://doi.org/10.1016/S0965-1748(00)00178-8)



- Madeja, M. 2000. Extracellular surface charges in voltage-gated ion channels. *News Physiol. Sci.* 15:15–19. <https://doi.org/10.1152/physiologyonline.2000.15.115>
- Moran, Y., M.G. Barzilay, B.J. Liebeskind, and H.H. Zakon. 2015. Evolution of voltage-gated ion channels at the emergence of Metazoa. *J. Exp. Biol.* 218:515–525. <https://doi.org/10.1242/jeb.110270>
- Neumaier, F., M. Dibué-Adjei, J. Hescheler, and T. Schneider. 2015. Voltage-gated calcium channels: Determinants of channel function and modulation by inorganic cations. *Prog. Neurobiol.* 129:1–36. <https://doi.org/10.1016/j.pneurobio.2014.12.003>
- Pavlov, E., C. Bladen, R. Winkfein, C. Diao, P. Dhaliwal, and R.J. French. 2005. The pore, not cytoplasmic domains, underlies inactivation in a prokaryotic sodium channel. *Biophys. J.* 89:232–242. <https://doi.org/10.1529/biophysj.104.056994>
- Peterson, B.Z., C.D. DeMaria, J.P. Adelman, and D.T. Yue. 1999. Calmodulin is the  $\text{Ca}^{2+}$  sensor for  $\text{Ca}^{2+}$ -dependent inactivation of L-type calcium channels. *Neuron.* 22:549–558. [https://doi.org/10.1016/S0896-6273\(00\)80709-6](https://doi.org/10.1016/S0896-6273(00)80709-6)
- Pitt, G.S., and S.Y. Lee. 2016. Current view on regulation of voltage-gated sodium channels by calcium and auxiliary proteins. *Protein Sci.* 25: 1573–1584. <https://doi.org/10.1002/pro.2960>
- Ramaswami, M., and M.A. Tanouye. 1989. Two sodium-channel genes in *Drosophila*: Implications for channel diversity. *Proc. Natl. Acad. Sci. USA.* 86:2079–2082. <https://doi.org/10.1073/pnas.86.6.2079>
- Reddi, R., K. Matulef, E.A. Riederer, M.R. Whorton, and F.I. Valiyaveetil. 2022. Structural basis for C-type inactivation in a Shaker family voltage-gated  $\text{K}^+$  channel. *Sci. Adv.* 8:eabm8804. <https://doi.org/10.1126/sciadv.abm8804>
- Rinkevich, F.D., Y. Du, and K. Dong. 2013. Diversity and convergence of sodium channel mutations involved in resistance to pyrethroids. *Pestic. Biochem. Physiol.* 106:93–100. <https://doi.org/10.1016/j.pestbp.2013.02.007>
- Rinkevich, F.D., Y. Du, J. Tolinski, A. Ueda, C.F. Wu, B.S. Zhorov, and K. Dong. 2015. Distinct roles of the DmNav and DSC1 channels in the action of DDT and pyrethroids. *Neurotoxicology.* 47:99–106. <https://doi.org/10.1016/j.neuro.2015.02.001>
- Rousset, M., C. Collet, T. Cens, F. Bastin, V. Raymond, I. Massou, C. Menard, J.B. Thibaud, M. Charreton, M. Vignes, et al. 2017. Honeybee locomotion is impaired by Am- $\text{Ca}_v3$  low voltage-activated  $\text{Ca}^{2+}$  channel antagonist. *Sci. Rep.* 7:41782. <https://doi.org/10.1038/srep41782>
- Salkoff, L., A. Butler, A. Wei, N. Scavarda, K. Giffen, C. Ifune, R. Goodman, and G. Mandel. 1987. Genomic organization and deduced amino acid sequence of a putative sodium channel gene in *Drosophila*. *Science.* 237: 744–749. <https://doi.org/10.1126/science.2441469>
- Salvage, S.C., Z.F. Habib, H.R. Matthews, A.P. Jackson, and C.L.H. Huang. 2021.  $\text{Ca}^{2+}$ -dependent modulation of voltage-gated myocyte sodium channels. *Biochem. Soc. Trans.* 49:1941–1961. <https://doi.org/10.1042/BST20200604>
- Sather, W.A., and E.W. McCleskey. 2003. Permeation and selectivity in calcium channels. *Annu. Rev. Physiol.* 65:133–159. <https://doi.org/10.1146/annurev.physiol.65.092101.142345>
- Sather, W.A., J. Yang, and R.W. Tsien. 1994. Structural basis of ion channel permeation and selectivity. *Curr. Opin. Neurobiol.* 4:313–323. [https://doi.org/10.1016/0959-4388\(94\)90091-4](https://doi.org/10.1016/0959-4388(94)90091-4)
- Shaya, D., F. Findeisen, F. Abderemane-Ali, C. Arrigoni, S. Wong, S.R. Nurva, G. Loussouarn, and D.L. Minor Jr. 2014. Structure of a prokaryotic sodium channel pore reveals essential gating elements and an outer ion binding site common to eukaryotic channels. *J. Mol. Biol.* 426:467–483. <https://doi.org/10.1016/j.jmb.2013.10.010>
- Shi, C., and N.M. Soldatov. 2002. Molecular determinants of voltage-dependent slow inactivation of the  $\text{Ca}^{2+}$  channel. *J. Biol. Chem.* 277: 6813–6821. <https://doi.org/10.1074/jbc.M110524200>
- Sigel, E. 1987. Properties of single sodium channels translated by *Xenopus* oocytes after injection with messenger ribonucleic acid. *J. Physiol.* 386: 73–90. <https://doi.org/10.1113/jphysiol.1987.sp016523>
- Sutro, J.B. 1986. Kinetics of veratridine action on Na channels of skeletal muscle. *J. Gen. Physiol.* 87:1–24. <https://doi.org/10.1085/jgp.87.1.1>
- Tadross, M.R., I.E. Dick, and D.T. Yue. 2008. Mechanism of local and global  $\text{Ca}^{2+}$  sensing by calmodulin in complex with a  $\text{Ca}^{2+}$  channel. *Cell.* 133: 1228–1240. <https://doi.org/10.1016/j.cell.2008.05.025>
- Tan, X.F., C. Bae, R. Stix, A.I. Fernández-Mariño, K. Huffer, T.H. Chang, J. Jiang, J.D. Faraldo-Gómez, and K.J. Swartz. 2022. Structure of the Shaker Kv channel and mechanism of slow C-type inactivation. *Sci. Adv.* 8:eabm7814. <https://doi.org/10.1126/sciadv.abm7814>
- Tang, L., T.M. Gamal El-Din, J. Payandeh, G.Q. Martinez, T.M. Heard, T. Scheuer, N. Zheng, and W.A. Catterall. 2014. Structural basis for  $\text{Ca}^{2+}$  selectivity of a voltage-gated calcium channel. *Nature.* 505:56–61. <https://doi.org/10.1038/nature12775>
- West, J.W., D.E. Patton, T. Scheuer, Y. Wang, A.L. Goldin, and W.A. Catterall. 1992. A cluster of hydrophobic amino acid residues required for fast  $\text{Na}^+$ -channel inactivation. *Proc. Natl. Acad. Sci. USA.* 89:10910–10914. <https://doi.org/10.1073/pnas.89.22.10910>
- Wu, J., Z. Yan, Z. Li, X. Qian, S. Lu, M. Dong, Q. Zhou, and N. Yan. 2016. Structure of the voltage-gated calcium channel  $\text{Ca}_v1.1$  at 3.6 Å resolution. *Nature.* 537:191–196. <https://doi.org/10.1038/nature19321>
- Yang, J., P.T. Ellinor, W.A. Sather, J.F. Zhang, and R.W. Tsien. 1993. Molecular determinants of  $\text{Ca}^{2+}$  selectivity and ion permeation in L-type  $\text{Ca}^{2+}$  channels. *Nature.* 366:158–161. <https://doi.org/10.1038/366158a0>
- Zhang, T., Z. Wang, L. Wang, N. Luo, L. Jiang, Z. Liu, C.-F. Wu, and K. Dong. 2013. Role of the DSC1 channel in regulating neuronal excitability in *Drosophila melanogaster*: Extending nervous system stability under stress. *PLoS Genet.* 9:e1003327. <https://doi.org/10.1371/journal.pgen.1003327>
- Zhao, Y., G. Huang, J. Wu, Q. Wu, S. Gao, Z. Yan, J. Lei, and N. Yan. 2019. Molecular basis for ligand modulation of a mammalian voltage-gated  $\text{Ca}^{2+}$  channel. *Cell.* 177:1495–1506.e12. <https://doi.org/10.1016/j.cell.2019.04.043>
- Zhou, W., I. Chung, Z. Liu, A.L. Goldin, and K. Dong. 2004. A voltage-gated calcium-selective channel encoded by a sodium channel-like gene. *Neuron.* 42:101–112. [https://doi.org/10.1016/S0896-6273\(04\)00148-5](https://doi.org/10.1016/S0896-6273(04)00148-5)